Biolocomotion near free surfaces in Stokes flows: mechanism of swimming and optimization

MASSACHUSETTS INSTITUTE
OF TECHNOLOGY
LIBRARIES

ARCHIVES

by

Sungyon Lee

Submitted to the Department of Mechanical Engineering
in partial fulfillment of the requirements for the degree of

Doctor of Philosophy in Mechanical Engineering

at the

MASSACHUSETTS INSTITUTE OF TECHNOLOGY

February 2010

© Massachusetts Institute of Technology 2010. All rights reserved.

Author ....
Department of Mechanical Engineering
December 10, 2009

Certified by ....
Anette E. Hosoi
Associate Professor, Mechanical Engineering
Thesis Supervisor

Accepted by ....
David E. Hardt
Chairman, Committee on Graduate Students

MASSACHUSETTS INSTITUTE
OF TECHNOLOGY
MAY 05 2010
LIBRARIES

Biolocomotion near free surfaces in Stokes flows: mechanism of swimming and optimization

by

Sungyon Lee

Submitted to the Department of Mechanical Engineering
on December 10, 2009, in partial fulfillment of the
requirements for the degree of
Doctor of Philosophy in Mechanical Engineering

Abstract

Locomotion of biological systems have fascinated physicists and engineers alike for centuries. In particular, we are interested in the motion of self-propelling bodies near an air-water interface in the low Reynolds number limit. To investigate this problem, we take two very different approaches. We first consider the locomotion of a specific organism, namely, a water snail, that exhibits a striking ability to "crawl" beneath the free surface. By modeling the foot of the snail as undergoing a simple sinusoidal motion, we apply lubrication approximations for small deformations to rationalize this peculiar mode of transport and its dependency on surface tension. Inspired by this study, the second part of my thesis focuses on the general two-dimensional model of an organism that utilizes a free surface to propel itself. Based on conformal mapping techniques, we are able to derive exact solutions describing the highly nonlinear coupling between the motion of the swimmer and the free surface deformations, without putting any limits on the deformation size. These closed-form solutions are then applied to optimization questions. In the high Reynolds number limit, swimming near the free surface is known to increase drag on the swimmer due to the cost associated with creating surface waves. However, we find that, for a low Reynolds number swimmer that utilizes the free surface to move, a different power law relation between the distance from the interface and the swimming efficiency exists, implying that the presence of the free surface can be beneficial in certain parameter regimes.

Thesis Supervisor: Anette E. Hosoi
Title: Associate Professor, Mechanical Engineering

Acknowledgments

I wish I could come up with a concise way to sum up my last five and half years here at MIT. For sure, it was humbling, eye-opening, fun, at times heart-breaking, and at other times exhilarating. I don't yet understand where this degree will take me. But I know for sure (despite sounding like a complete "cheese-ball"), I'll take my experience here and all the people who entered my life with me, wherever I may go and whatever I may end up doing.

I want to especially thank...

- my amazing advisor, Prof. Peko Hosoi, who does it all while making it look so easy and without losing a smile on her face,
- my committee members and collaborators who have challenged me in ways that I didn't know I could be challenged,
- Ms. Debbie Blanchard who provided me with chocolate, a place to hide, and many reasons to laugh and to keep going,
- my labmates who put up with my sarcasm,
- my roommates on Lopez Street who became my alternate family unit away from home,
- my community group and all my friends whose love and prayers I cannot even begin to pay back,
- Gus' Toscannis, my home away from home,
- Tony Yu who played all three roles of a labmate/roommate/friend the whole time and did it without us killing each other,
- my family who I miss and love everyday,
- and finally, the One and Only without whom I am utterly lost.

Really, thank you, from the bottom of my heart.

Contents

1 Introduction **15**

2 Water snail locomotion **19**

- 2.1 Observations 21
- 2.2 Model 23
  - 2.2.1 Assumptions 23
  - 2.2.2 General equations 23
  - 2.2.3 Lubrication Analysis 24
  - 2.2.4 Solution for small-amplitude motion 28
  - 2.2.5 Boundary conditions 29
  - 2.2.6 Crawling speed 32
  - 2.2.7 Results 32
  - 2.2.8 Matching internal and external flows 38
- 2.3 Discussion 40

3 Point Swimmer **43**

- 3.1 Conformal map 44
- 3.2 Governing equations — complex variables 46
- 3.3 The swimmer — singularity description 48
- 3.4 Swimming beneath free surface — conformal map approach 50
  - 3.4.1 General solutions 50
  - 3.4.2 Complete solution: n=1 56

4 Optimal swimming near free surfaces 67
4.1 Optimization in low Reynolds locomotion 67
4.2 Mathematical setup 69
4.2.1 Calculating and minimizing the rate of viscous dissipation . . 69
4.3 Results 71
4.3.1 Proximity to the interface 71
4.3.2 Optimal free surface shapes 72
4.4 Discussion 80

5 Conclusion 83

A Details from the point swimmer 87
A.1 Far field condition 87
A.2 Steady swimming beneath a flat interface: method of images 89

B Calculating the rate of viscous dissipation 93

C Details from the optimization 97
C.1 Full equations 97
C.1.1 Asymptotics 99

List of Figures

2.1.1 Snail (*Sorbeoconcha physidae*) crawling smoothly underneath the water surface while the surface deforms. Note the surface deflection associated with the undulatory waves propagating from nose to tail along its foot. Photo courtesy of David Hu and Brian Chan (MIT). 22

2.1.2 A trail of mucus behind the snail crawling upside down beneath the free surface. Photo courtesy of David Hu and Brian Chan (MIT). . . 22

2.2.1 A close-up view of the mucus and the snail foot undergoing a simple sinusoidal deformation of wavelength $\widehat{2\pi\lambda}$. The prescribed shape of the snail foot is denoted as $\widehat{h_1}$; the resultant shape of the free surface, $\widehat{h_2}$, is to be solved for. The known constant speed of the wave, $\widehat{V_w}$, is set relative to the snail that is translating with an unknown speed, $\widehat{V_s}$. In the laboratory frame (a), the wave is moving in the negative $\widehat{x}$-direction with $\widehat{V_w} - \widehat{V_s}$ while the snail is moving in the positive $\widehat{x}$-direction with $\widehat{V_s}$. In the frame moving with the wave (b), the snail body appears to move in the positive $\widehat{x}$-direction with $\widehat{V_w}$. 25

2.2.2 Free body diagram of a perfectly periodic mucus layer over one wavelength between nodes j and $j+1$. Pressures at these nodes, $p(2\pi j)$ and $p(2\pi(j+1))$, as well as the heights, $h_2(2\pi j)$ and $h_2(2\pi(j+1))$, are equal by the periodic boundary conditions. Above the mucus layer is open to atmosphere with p_{atm} set to zero. 30

2.2.3 (a) Dimensionless propulsive force, F_{prop}, normalized by the number of wavelengths, n, as a function of the modified capillary number, $\widetilde{Ca} \equiv \mu\widehat{V}_w/a^3\sigma$, where the values of n range from 5 to 30 in increments of 5. In (b) and (c), the absolute value of the dimensionless force, F_{prop}, is plotted on a logarithmic scale to show the power-law decay in the limits of $\widetilde{Ca} \rightarrow 0$ and $\widetilde{Ca} \rightarrow \infty$ respectively. The propulsive force exhibits a $\widetilde{Ca}^{-1}$ decay for large $\widetilde{Ca}$, while it decays as $\widetilde{Ca}^{3}$ for small $\widetilde{Ca}$. 33

2.2.4 Absolute magnitudes of components of dimensionless propulsive force due to pressure (solid line) and due to shear (dashed line) as a function of $\widetilde{Ca}$ for $n = 10$. (note that the shear force is negative). Hence, the total propulsive force which is the sum of these two forces is non-zero only when there is a difference between the two. 34

2.2.5 Dimensionless pressure (a, dashed line) and shear stress (b, dashed line) within the mucus over two wavelengths for $n = 10$. The single dotted line in both (a) and (b) is the shape of the foot, h_1 while the solid lines describe the shape of the interface, h_2 for different values of $\widetilde{Ca}$. Black arrows indicate the direction of increasing $\widetilde{Ca}$. 35

2.2.6 Dimensionless pressure (dashed line) and the interface shape (solid line) in the front (a) and end (b) of the snail for $n = 10$. The dotted line is the shape of the foot, and black arrows are in the direction of decreasing surface tension. 36

2.2.7 Free body diagram of an asymmetric mucus layer across the foot of the snail. (For simplicity, $n = 1$ in this diagram.) Pressures at the ends, $p(0)$ and $p(2n\pi)$ are equal by the boundary condition; however, they act over two different mucus thicknesses, resulting in a net pressure force. 37

2.2.8 Schematic of the snail with three distinct flow regions. The layer of mucus above the snail foot is denoted as 'internal' while the ambient flow around the snail's body is 'external.' The two dashed boxes (labeled A) enclose the matching regions that connect the internal and external flows. 37

3.3.1 The idea of the singularity model: a finite-body swimmer beneath a free surface is modelled as a point stresslet singularity. 48

3.4.1 Conformal mapping $z(\zeta)$ from the unit ζ-disc to the fluid region beneath the interface. In this mapping, $\zeta = 0$ maps to the swimmer at $z = z_d$, and $\zeta = -\mathrm{i}$ maps to the interface at infinity. The variable s denotes the arclength and is defined positive going from positive to negative infinity. 51

3.4.2 The geometrical significance of parameters a and c for $n = 1$. The flat interface corresponds to $a = 2, c = 0$. Increasing (decreasing) a above 2 with $c = 0$ (along the horizontal axis) moves the interface up (down) in a left-right symmetric fashion. Non-zero values of c (along the vertical axis) introduce left-right asymmetry. 56

3.4.3 For an interface shape $a = 2.1$ and $c = 0.1$ ($n = 1$), the corresponding functions $f(z)$ and $g'(z)$ are shown in (a) and (b), respectively. 60

3.4.4 For an interface shape $a = 2.1$ and $c = 0.1$ ($n = 1$), the resulting streamlines are plotted in (b). The flow inside the domain is described completely by two complex functions, f and g, obtained analytically using the conformal mapping technique. The resultant pressure field as well as the vorticity field is shown in (a). Note that low pressure underneath the "bump" is generated by viscous stresses that dominate over capillary effects, as illustrated in (c). 61

3.4.5 The singularity strengths, (a) stresslet $|s^*|$ (b) dipole $|d^*|$ and and (c) quadrupole $|q^*|$ as the interface transitions from a downward deformation ($a < 2$) to an upward deformation ($a > 2$) with $c = 0$. Note that the quadrupole is absent ($q^* = 0$) when $a = 2$ (the flat interface case) but its strength increases for $a \neq 2$ (the deformed interface case). . . 62

3.4.6 The swimmer creates a local flow by "squirming", represented mathematically by singularities (i.e. for $n = 1$, a stresslet, dipole, and quadrupole). Depending on the fluid properties such as surface tension σ and viscosity μ, this local flow interacts with the free surface, and this interplay advects the swimmer. Thus, the arrow (i) represents a "forward" (analysis) approach to the problem. However, we solve the *inverse* (synthesis) problem (represented by arrow (ii)). 64

3.4.7 The solutions $f(z)$ and $g(z)$ for a flat interface $a = 2$ and $c = 0$ ($n = 1$) are shown in (a) and (b), respectively. These plots can be thought of the effective behaviors of the singularities of $f(z)$ and $g(z)$, in this case, a stresslet and a potential dipole 64

4.1.1 (a) Purcell's three-link swimmer, as introduced in his lecture, consists of three rods and can generate non-reciprocal motion by moving the rods alternatively (image reproduced from [56]. One example of a swimming sequence is shown in (b) [7]. 68

4.3.1 The rate of minimum dissipation, E_{min}, in the system is shown to vary as R^{-4} (where R is the "cutoff" radius), independent of the the capillary number, Ca. 71

4.3.2 The value of $\Delta a_{\text{opt}} \equiv 2 - a_{\text{opt}}$, the measure of deviation from the flat interface, as a function of the capillary number, Ca for different values of R. As expected, in the limit of low Ca (high surface tension) as well as $R \to 0$, the interface remains flat (i.e. $\Delta a_{\text{opt}} = 0$, $c = 0$). As Ca increases (low surface tension), a small dip ($\Delta a_{\text{opt}} > 0$) begins to grow. As Ca continues to increase, this deflection saturates at some maximum Δa_{opt} value that varies with R. The free surface shapes that correspond to the most energy efficient steady state solutions as a function of capillary number, Ca are shown in the inset. In all cases, c_{opt}, the measure of asymmetry, remains approximately zero. 73

4.3.3 The value of Δa_{opt} shares the common trend of starting off at 0 and decreasing until it saturates at some maximum value. The two distinct transitions (from flat to deformed, and from deformed to maximum deformation) are marked by two sets of critical capillary numbers, as plotted here for varying values of the cutoff radius R. These critical values, $\mathrm{Ca}_{\mathrm{crit},1}$ and $\mathrm{Ca}_{\mathrm{crit},2}$, both increase linearly with R. 74

4.3.4 The dependance of the deformation size on the characteristic swimmer size is demonstrated for two different relative values of R. 74

4.3.5 The rates of viscous dissipation for an asymptotically small bump up (dashed) and down (dotted) are plotted against the cutoff radius R, confirming that the bump down is more energetically favorable. Since this plot includes only the first order effects of the small perturbation solutions, it highlights the usefulness of the asymptotic analysis in predicting the physical results. 75

4.3.6 Deforming the interface downwards can be interpreted as bringing the image singularity closer to the swimmer. The flow is generated by the interaction between the swimmer and its image, which consequently induces the horizontal motion of the swimmer. Thus, with the image singularity closer to the swimmer, smaller singularity strengths yield the same horizontal speed (leading to reduced dissipation). However, there is also an energetic cost of deforming the interface downwards. This competition explains why the optimal downward deformation does not grow indefinitely but saturates at a critical capillary number. . . 76

4.3.7 The deviation from the flat interface, $2 - a_{\mathrm{opt}}$, is denoted as $\Delta\widetilde{a}_{\mathrm{opt}}$ after it has been scaled by R^2. Similarly, $\widetilde{\mathrm{Ca}} \equiv \frac{\mathrm{Ca}}{R}$ is the rescaled capillary number. This particular pair of rescaling results in collapsing Δa_{opt} versus Ca plots into one curve, from which one can extract interesting scaling relations. (The numerical data for small $\widetilde{\mathrm{Ca}}$ is better shown in the inset (a) on a linear vertical scale.) Three distinct regimes emerge from this plot, denoted as [A], [B], and [C]. The regime [A] corresponds to the flat interface as the optimal free surface shape, and [B] shows the optimal deformation growing with surface tension, while the last regime [C] is the optimal deformation saturated at a maximum value. 77

4.3.8 An approximate expression for $\Delta\widetilde{a}_{\mathrm{opt}}$ (plotted as dotted lines) is derived from asymptotic solutions and shows a good overall agreement with the full solutions, despite a clear shift at the transition from flat to deformed interfaces ($\mathrm{Ca}_{\mathrm{crit1}}$). 78

A.2.1 The method of images: to satisfy the boundary condition on the free surface an image singularity must be introduced at the reflection of the point swimmer position. 89

C.1.1 Considering the asymptotic solutions to $O(\varepsilon^2)$ allows one to predict the values of $\mathrm{Ca}_{\mathrm{crit1}}$ for varying R, as plotted here. (The solid dots correspond to the asymptotic equations, while the empty squares are the full results.) The asymptotic solutions are in a good agreement with the exact equations, but they tend to be consistently lower. . . . 102

Chapter 1

Introduction

Locomotion of biological systems through different fluid media is an active area of research for physicists and engineers alike. The motivation for such study varies widely from a simple curiosity about how organisms move to a more practical one, namely, taking cues from nature to engineer better systems. One commonplace example of locomotion is swimming. Often one is interested in reducing drag to enable more efficient locomotion. For instance, much research is being conducted to design a better swimsuit to reduce drag for elite swimmers [69, 64, 70, 8, 21, 17]. The magnitude of the drag force is not only a product of the swimmer's inherent properties (i.e., its shape and skin texture) but also depends largely on the external factors, such as the fluid properties and surrounding geometry. One particular environmental factor we are interested in is the presence of an air-water interface, since different biological swimmers, ranging from humans to eels, are often observed to swim near the free surface [32]. This seemingly innocuous act of being close to the free surface tends to increase drag for swimmers of moderate to large Reynolds numbers, where the Reynolds number (Re) is the ratio of inertial to viscous effects [32].

With advances in technology that allow one to investigate a world at a microscopic level, we can now ask the same set of questions about both biological and man-made swimmers on much smaller scales [25]. Termed low Re swimmers, these tiny organisms occupy a world much different from their high Re counterparts and are subject to various challenges associated with propulsion [68, 56, 42, 10, 13, 18]. Any time reversible or reciprocal motion generated by these swimmers, isolated in an unbounded fluid, cannot give rise to locomotion. This constraint is known as the Scallop Theorem [56]. Going back to locomotion near the free surface, we are especially interested in how low Re swimmers transport themselves under the influence of surface tension in this inertialess world. More specifically, we investigate here a kind of low Re swimmers that *utilize* the presence of the free surface to move forward. Within this framework, the influence of the free surface on the swimming efficiency may be favorable, contrary to what is commonly known for high Re swimmers. In other words, the swimmer's proximity to the free surface may be more energetically favorable for its locomotive efficiency. Furthermore, we calculate the swimming protocols and corresponding free surface shapes that *minimize* the viscous drag.

We begin by looking at nature and considering a specific organism that employs a very curious mode of locomotion near the air-water interface. Some freshwater and marine snails have been observed to "crawl" underneath the free surface that is unable to sustain shear stresses [14, 47, 29, 22, 19, 20]. A specific type of water snails that we study — *Sorbeoconcha physidae* — is believed to undulate its foot in some fashion and consequently deform the free surface above. It also leaves a trail of mucus when it travels, leading one to postulate that a thin layer of mucus exists between the foot of the snail and the free surface at all times. Based on these observations, we develop a two-dimensional lubrication model for the surface tension driven flow inside the thin mucus layer and tie it to the external flow around the snail to derive the relationship between the propulsion of the snail and the shape of the interface [39].

Motivated by the study of water snails, we then consider a completely general swimmer that is not constrained by geometrical factors, such as a thin layer of fluid between the free surface and the swimmer. Instead, we look at a swimmer in a semi-infinite fluid bounded by an air-water interface, again in two dimensions. Because we are more interested in the large-scale flow field generated by this swimmer, rather than the detailed swimming patterns, we model the swimmer as a sum of mathematical singularities. These simplifications allow us to employ conformal mapping techniques, in which we use a known invertible map $z(\zeta)$ that relates the physical space z to the conformal space ζ, the unit circle. Then in this conformal space, we can obtain exact solutions describing the flow and map them back to the physical domain. Once these solutions are known, one can delve deeper into a number of interesting problems, such as the energetic cost associated with this type of locomotion.

In the limit of low Reynolds number, the presence of the free surface can be used to give rise to propulsion. This thesis consists of two different approaches to this problem — one that considers a specific organism and a simplified mathematical model (Chapter 2), and the other that explores a more general and robust mathematical analysis of swimming near the free surface (Chapter 3). The first part satisfies the scientist's curiosity of finding problems in nature and figuring out how a particular swimmer achieves its motion. The latter provides a more rigorous framework to understand free surface swimming that can potentially be used to manipulate the presence of interfaces for more efficient locomotion. This question of efficiency and optimization is investigated in Chapter 4, followed by a conclusion in Chapter 5.

Chapter 2

Water snail locomotion

[1]Engineers often look to nature's wide variety of locomotion strategies to inspire new inventions and robotic devices [11, 16, 1, 53]. More generally, scientists across all disciplines are interested in understanding the physical mechanisms behind different styles of biolocomotion. The mechanism of terrestrial snail locomotion has been investigated and elucidated over the last couple of decades; conversely, the propulsion of water snails that crawl beneath a free surface has yet to be considered. The purpose of this chapter is to propose a propulsive mechanism for water snails.

Gastropod locomotion has been of scientific interest for more than a century [63, 72, 50]. Three distinct modes of locomotion have been examined: ciliary motion, pedal waves, and swimming. Ciliary locomotion, characterized by the beating of large arrays of cilia on the animal's foot, is usually distinguished from pedal waves by indirect means, such as lack of visible muscle undulation, uniform adherence of the foot to the substrate, and a uniform gliding of the snail body [4]. This particular type of locomotion is mostly employed by various marine and freshwater snails.

A significant effort has gone towards understanding pedal wave locomotion by terrestrial snails. Lissmann [44, 45] was a pioneer in constructing a mechanistic model of the snail foot undergoing such locomotion. In Ref. [44], he studied three species of terrestrial snails (*Helix*, *Haliotis*, and *Pomatias*), all of which use waves of contraction that propagate in the direction of their motion ("direct waves"). Waves traveling in the opposite direction ("retrograde waves") were examined by Jones and Trueman [34]. A vital insight was later provided by Denny [23], who turned the focus of study from the snail foot to the properties of the pedal mucus. Pedal mucus has a finite yield stress that allows it to act as an adhesive under small strains and to flow like a viscous liquid beyond its yield point. Thus, the snail is able to create regions of flow in the mucus by locally shearing it while the rest of the mucus is effectively glued to the solid substrate; these regions (or shear waves) propagate along the length of the foot, enabling the snail to move. Denny used the nonlinear nature of the mucus to rationalize the locomotion of *Ariolimax columbianus*, a terrestrial slug [24]. Recently, it was found that mucus with shear-thinning properties results in energetically favorable locomotion [37], which is well-supported by experimental studies of the mucus properties. A detailed investigation of the rheology of mucus was conducted by Ewoldt *et al.* [26], who also tested different synthetic slimes. The versatility of snail locomotion also inspired Chan *et al.* [16] to build a robotic snail, the first mechanical device to utilize the nonlinear properties of this synthetic mucus.

---

[1] This chapter appeared as Crawling beneath the free surface: Water snail locomotion in Physics of Fluids 20, 082106 (2008).

Terrestrial snails that employ adhesive locomotion are only a fraction of species in the class of gastropods. Traditionally, gastropods have been divided into four subclasses: prosobranchia, opisthobranchia, gymnomorpha, and pulmonata, the latter of which consists primarily of terrestrial snails. Many species have not been thoroughly investigated but exhibit interesting locomotive behavior. For instance, opisthobranchs, that have reduced or absent shells, swim [27] or burrow [2, 3]. A still more puzzling mode of locomotion is observed in certain species of water snails.

In 1910, Brocher [14] remarked on water snails that can swim inverted beneath the water surface; since then, other qualitative descriptions have been reported. Milnes and Milnes [47] observed the foot of a pond snail "pulsing with slow waves of movement from aft to fore along its length," suggesting that direct waves are employed for propulsion. The presence of a trail of snail mucus was also reported. Goldacre [29] measured the surface tension of this thin trailing film to be approximately 10 dynes/cm; he also remarked that the creature was "grasping the film" as evidenced by the film's being pushed sideways as the snail advanced. Deliagina and Orlovsky [22] made similar observations while studying feeding patterns of *Planorbis corneus.* This particular freshwater snail crawls at about 15 mm/s, a speed comparable to that on land, while the cilia apparent on the organism's sole "beat intensely." Cilia-aided crawling beneath a free surface was observed on marine snails as early as 1919. Copeland [19] concluded that the locomotion of *Alectrion trivittata*, which crawls upside down on the surface, relied solely on the ciliary action. He conducted a similar study on *Polinices duplicata* and *Polinices heros*, both of which were observed to use both cilia and muscle contraction for locomotion on hard surfaces [20]. Only ciliary motion was employed by the young *Polinices heros* when crawling inverted beneath the surface.

It is therefore clear that freshwater and some marine snails have the striking ability to move beneath a surface that is unable to sustain shear stresses. In this chapter, we attempt a first quantitative rationalization of these observations. We use a simplified model based on the lubrication approximation to show that a free-moving organism located underneath a free surface can move using traveling-wave-like deformations of its foot. We first present our observations of the propulsion of the freshwater snail, *Sorbeoconcha physidae* in §2.1. We introduce our model based on the lubrication approximation in §2.2, and present solutions for small-amplitude motion of the foot. The physical picture for the generation of propulsive forces is discussed in §2.3, together with the main conclusions and a summary of the simplifying assumptions used in our analysis.

2.1 Observations

Several common freshwater snails, *Sorbeoconcha physidae*, were collected from Fresh Pond, Massachusetts. About 1 cm in length, this particular snail can crawl beneath the water surface at speeds as high as 0.2 cm/s, comparable to its speed on solid substrates, and perform a 180° turn in 3 seconds. It is rendered neutrally buoyant by trapping air in its shell.

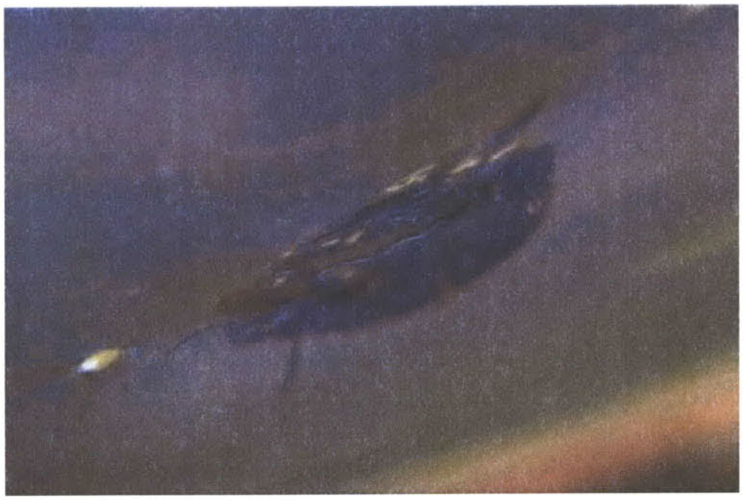

Figure 2.1.1: Snail (*Sorbeoconcha physidae*) crawling smoothly underneath the water surface while the surface deforms. Note the surface deflection associated with the undulatory waves propagating from nose to tail along its foot. Photo courtesy of David Hu and Brian Chan (MIT).

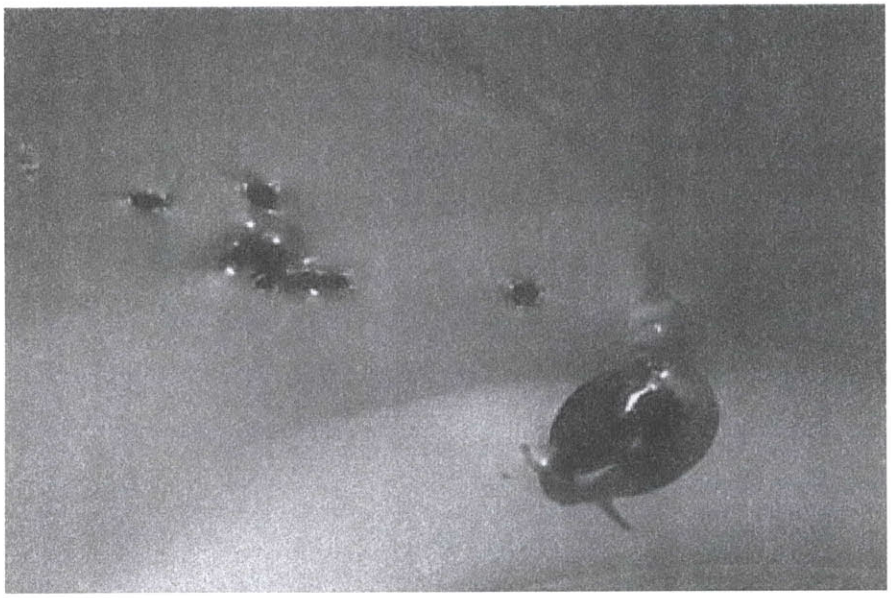

Figure 2.1.2: A trail of mucus behind the snail crawling upside down beneath the free surface. Photo courtesy of David Hu and Brian Chan (MIT).

The undulation of the snail foot causes surface deformations with a characteristic wavelength of 1 mm and amplitude of 0.2 – 0.3 mm (see Figure 2.1.1). This deformation appears to travel in the opposite direction of the snail motion, suggesting the generation of retrograde waves, contrary to observations of Milnes and Milnes [47].

Another notable feature of water snail propulsion is the presence of a trail of mucus (see Figure 2.1.2). For land snails, this mucus layer is typically $10-20\,\mu$m in thickness [26]; as with land snails, its rheological characteristics may also play a significant role in underwater locomotion. Since these water snails are also able to crawl on solid substrates, one might venture that their mucus properties do not differ too greatly from those of land snails.

2.2 Model

2.2.1 Assumptions

The crawling of water snails beneath the free surface has four distinct physical features: a free surface with finite surface tension, σ, a layer of (presumably) non-Newtonian mucus, coupled deformations of the foot and the surface, and a matching of the flow inside the mucus to that around the snail. To isolate the critical influence of the first feature, we consider in this paper a simplified model system characterized by a Newtonian mucus layer and small deformations of the foot and the interface, with hopes of providing physical insight into the propulsion mechanism.

2.2.2 General equations

Choosing a characteristic velocity $U \sim 1\,\text{cm/s}$, a mucus thickness $H \sim 20\,\mu\text{m}$, and a (post-yield) mucus viscosity $\nu \sim 10^{-2}\,\text{m}^2/\text{s}$ [26] suggests a Reynolds number of the flow within the mucus layer to be $\text{Re} \equiv UH/\nu \sim 10^{-5}$. Thus, we neglect inertia and start with incompressible Stokes equations:

$$\nabla \cdot \mathbf{v} = 0, \qquad \nabla \cdot \mathbf{\Pi} = 0, \tag{2.2.1a, b}$$

where $\mathbf{v}$ is the velocity field inside the mucus and $\mathbf{\Pi}$ the stress tensor. Normal and tangential stress boundary conditions at the surface may be expressed as

$$\mathbf{n} \cdot \mathbf{\Pi} \cdot \mathbf{n} = \sigma\widehat{\kappa}, \qquad \mathbf{t} \cdot \mathbf{\Pi} \cdot \mathbf{n} = 0, \tag{2.2.2a, b}$$

where $\mathbf{n}$ and $\mathbf{t}$ denote, respectively, unit vectors normal (outward) and tangent to the free surface, and $\widehat{\kappa} = -\nabla \cdot \mathbf{n}$, denotes the curvature of free surface. We limit our attention to the two-dimensional case, for which the interface shape is given by $\widehat{y} = \widehat{h}(\widehat{x})$ (see Figure 2.2.1) and $\widehat{\kappa}$ may be expressed as $\widehat{h}_{\widehat{x}\widehat{x}}/(1+\widehat{h}_{\widehat{x}}^2)^{3/2}$, where the "hat" notation denotes dimensional variables. The mucus is assumed to be a Newtonian fluid; thus, the stress tensor is given by

$$\mathbf{\Pi} = -\widehat{p}\mathbf{I} + 2\mu \boldsymbol{e}, \tag{2.2.3}$$

where $\boldsymbol{e} \equiv \frac{1}{2}\{(\nabla \mathbf{v}) + (\nabla \mathbf{v})^{\mathrm{T}}\}$ is the rate-of-strain tensor.

In the frame moving with the snail, we assume that the gastropod foot undergoes periodic deformations in the form of a traveling wave moving at a speed $\widehat{V}_w$. Our approach is as follows: given the shape of the foot, we solve for the shape of the liquid-air interface together with the velocity field in the mucus layer, and then calculate the resulting propulsive force on the snail.

2.2.3 Lubrication Analysis

To eliminate temporal variation, we consider the frame of reference moving at the wave speed $\widehat{V}_w$ relative to the snail (Fig. 2.2.1). We define $\widehat{V}_w$ and the (unknown) snail speed, $\widehat{V}_s$, to be positive when the snail moves in the positive $\widehat{x}$-direction while the wave travels in the opposite direction.

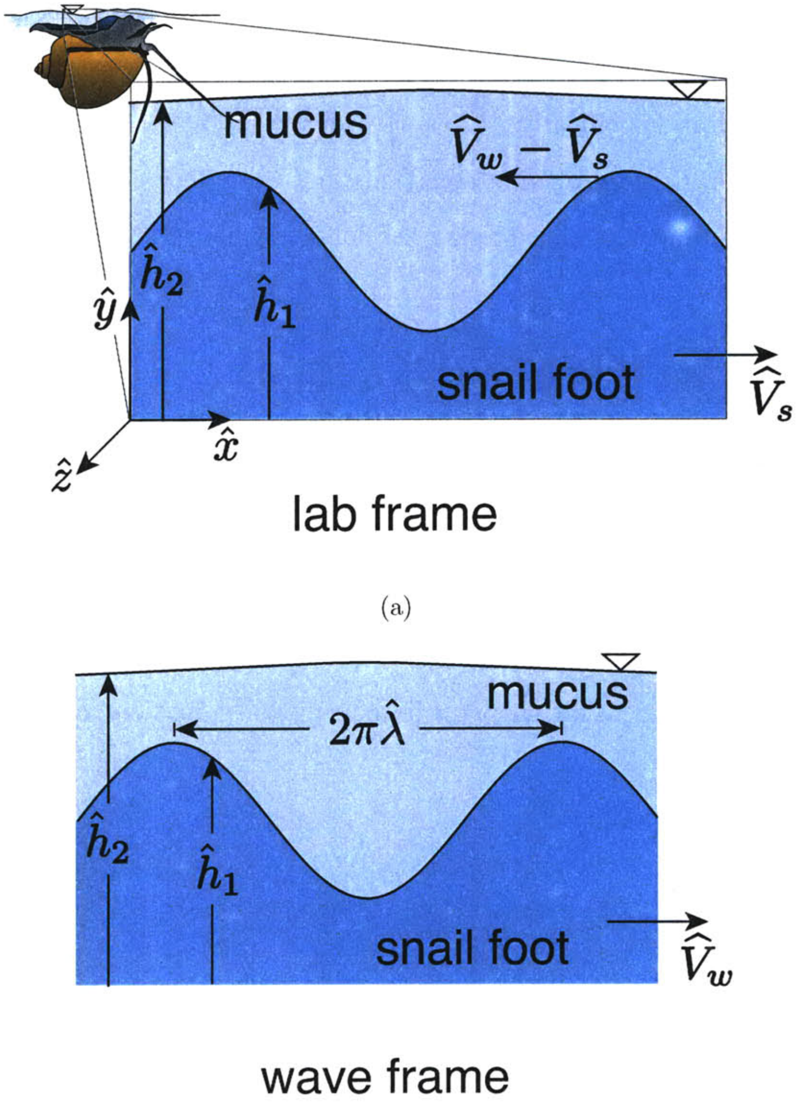
mucus
$\widehat{V}_w - \widehat{V}_s$
$\hat{h}_2$
$\hat{h}_1$
$\hat{y}$
snail foot
$\widehat{V}_s$
$\hat{x}$
$\hat{z}$
lab frame
mucus
$2\pi\hat{\lambda}$
$\hat{h}_2$
$\hat{h}_1$
snail foot
$\widehat{V}_w$
wave frame

(a)

(b)

Figure 2.2.1: A close-up view of the mucus and the snail foot undergoing a simple sinusoidal deformation of wavelength $2\pi\widehat{\lambda}$. The prescribed shape of the snail foot is denoted as $\widehat{h}_1$; the resultant shape of the free surface, $\widehat{h}_2$, is to be solved for. The known constant speed of the wave, $\widehat{V}_w$, is set relative to the snail that is translating with an unknown speed, $\widehat{V}_s$. In the laboratory frame (a), the wave is moving in the negative $\widehat{x}$-direction with $\widehat{V}_w - \widehat{V}_s$ while the snail is moving in the positive $\widehat{x}$-direction with $\widehat{V}_s$. In the frame moving with the wave (b), the snail body appears to move in the positive $\widehat{x}$-direction with $\widehat{V}_w$.

The thickness of the mucus (tens of microns) is observed to be small relative to a typical wavelength of foot deformation (millimeters). Thus, we apply the lubrication approximation [57, 48, 49, 38] and reduce the governing equations based on $\widehat{H}/\widehat{\lambda} \equiv a \ll 1$, where $\widehat{H}$ is the characteristic thickness of the mucus film, and $\widehat{\lambda}$ the wavelength divided by 2π. More specifically, terms of order a or higher are discarded in the equations of motion. The governing equations and boundary conditions (Eq. 2.2.1 - Eq. 2.2.3) are non-dimensionalized using the following set of characteristic scales:

$$\widehat{x} = \widehat{\lambda} x, \tag{2.2.4a}$$

$$\widehat{y} = \widehat{H} y, \tag{2.2.4b}$$

$$(\widehat{u}, \widehat{v}) = \widehat{V}_w (u, av), \tag{2.2.4c}$$

$$\widehat{V}_s = \widehat{V}_w V_s, \tag{2.2.4d}$$

$$\widehat{p} = \frac{\mu \widehat{\lambda} \widehat{V}_w}{\widehat{H}^2} p. \tag{2.2.4e}$$

Based on standard lubrication theory, the equations of motion are reduced to the following:

$$0 = \frac{\partial u}{\partial x} + \frac{\partial v}{\partial y}, \tag{2.2.5a}$$

$$0 = -\frac{\partial p}{\partial x} + \frac{\partial^2 u}{\partial y^2}, \tag{2.2.5b}$$

$$0 = \frac{\partial p}{\partial y}, \tag{2.2.5c}$$

while the boundary conditions may be expressed as

$$u = 1, \quad \text{at} \quad y = h_1, \tag{2.2.6a}$$

$$v = 0, \quad \text{at} \quad y = h_1, \tag{2.2.6b}$$

$$0 = \frac{\partial u}{\partial y}, \quad \text{at} \quad y = h_2, \tag{2.2.6c}$$

$$\frac{a^3}{\mathrm{Ca}} h_{2,xx} = -p, \quad \text{at} \quad y = h_2, \tag{2.2.6d}$$

where x and y are horizontal and vertical coordinates of the system while z points out of the page, and u and v are velocity components in x- and y-directions, respectively.

The shape of the snail foot is prescribed by $h_1(x)$ while $h_2(x)$ denotes the unknown free surface shape. Note that $\mathrm{Ca} \equiv \mu \widehat{V}_w / \sigma$ is not a capillary number in the traditional sense since $\widehat{V}_w$ is not necessarily the characteristic speed of the flow in the lubrication layer. In order to allow surface tension effects to remain relevant in the current problem, the curvature term in Eq. (2.2.6d) is retained despite being multiplied by a^3; this is a standard practice in thin film problems with surface tension (see, e.g., Goodwin and Homsy [30]).

For convenience, we define a modified capillary number, $\widetilde{Ca} \equiv \mu \widehat{V}_w / a^3 \sigma = \mathrm{Ca}/a^3$, so that the normal stress condition becomes

$$\frac{1}{\widetilde{Ca}} h_{2,xx} = -p, \quad \text{at} \quad y = h_2. \tag{2.2.7}$$

Then by integrating Eq. (2.2.5b) twice with respect to y, and applying necessary boundary conditions, we obtain an expression for the velocity field in the mucus layer,

$$u(x,y) = \frac{1}{\widetilde{Ca}} h_{2,xxx} \left(h_2 y - \frac{1}{2} y^2 + \frac{1}{2} h_1^2 - h_2 h_1 \right) + 1. \tag{2.2.8}$$

The resulting volume flux through the layer,

$$Q = h_2 - h_1 + \frac{1}{\widetilde{Ca}} h_{2,xxx} \left[\frac{1}{3} \left(h_2 - h_1 \right)^2 \left(\frac{1}{2} h_1 + h_2 \right) + h_1 \left(h_2 - h_1 \right) \left(\frac{1}{2} h_1 - h_2 \right) \right], \tag{2.2.9}$$

is constant since the mucus thickness does not vary with time in this moving reference frame.

In order to obtain the motion of the snail, it is necessary to consider the forces acting on the organism. Since its motion occurs at low Reynolds numbers, the snail is force-free; hence, the forces from the (internal) mucus flow and those from the external flow around the body must sum to zero:

$$\mathbf{F}_{\text{int}} + \mathbf{F}_{\text{ext}} = \mathbf{0}. \tag{2.2.10}$$

More specifically, $\mathbf{F}_{\text{ext}}$ is equal to $-\widehat{F}_{\text{drag}} \mathbf{e}_{\mathbf{x}}$, where $\widehat{F}_{\text{drag}}$ is the magnitude of the drag force from the external flow; $\mathbf{F}_{\text{int}}$ is the traction caused by the flow in the mucus on the foot of the snail and can be expressed as the integral of $\mathbf{\Pi} \cdot \mathbf{n}_f$, where $\mathbf{n}_f$ is outward normal to the foot of the snail. In the lubrication limit, Eq. (2.2.10) reduces to

$$\widehat{w}\left(\frac{\mu \widehat{V}_w}{a}\right) \int_0^{2n\pi} \left[p\frac{dh_1}{dx} + \left.\frac{du}{dy}\right|_{y=h_1}\right] dx = \widehat{F}_{\text{drag}}, \tag{2.2.11}$$

which is a scalar equation representing force-balance in the x-direction. Here n is the number of waves generated by the foot and $\widehat{w}$ is the width of the foot in the z-direction. Physically, the left hand side of Eq. (2.2.11) is the propulsive force that arises from the internal flow of the mucus and balances the drag from the external flow. Note that Eqs. (2.2.10)-(2.2.11) implicitly neglect the overlap regions between the internal mucus flow and the external flow around the organism; we will derive in §2.2.8 the asymptotic limit in which this is a valid assumption.

2.2.4 Solution for small-amplitude motion

In order to solve the model problem, we consider the following limit for foot deformations. If $\Delta\widehat{H}$ denotes the typical amplitude of the foot deformation, we define $\varepsilon \equiv \Delta\widehat{H}/\widehat{\lambda}$, and assume it to be small. Note that ε is a parameter independent of the geometrical aspect ratio, a, as can be seen by considering the case where $\varepsilon = 0$; in this limit, the dimensionless parameter, ε, is zero when the foot surface is flat, while a remains finite. We choose the foot shape as

$$h_1 = \varepsilon \sin x, \tag{2.2.12}$$

and solve for the associated layer profile, h_2, order by order as

$$h_2 = 1 + \varepsilon h_2^{(1)} + \varepsilon^2 h_2^{(2)} + O(\varepsilon^3). \tag{2.2.13}$$

The resulting expression for the flux is given by

$$\begin{aligned}
&\frac{Q}{1+\varepsilon\left(h_2^{(1)}-\sin x\right)+\varepsilon^2 h_2^{(2)}} = 1+ \\
&\frac{(\varepsilon h^{(1)}_{2,xxx}+\varepsilon^2 h^{(2)}_{2,xxx})}{\widetilde{Ca}}\left[\frac{1}{3}\left(1+\varepsilon\left(h_2^{(1)}-\sin x\right)+\varepsilon^2 h_2^{(2)}\right)^2\left(1+\varepsilon\left(h_2^{(1)}+\frac{1}{2}\sin x\right)+\varepsilon^2 h_2^{(2)}\right)\right]- \\
&\frac{(\varepsilon h^{(1)}_{2,xxx}+\varepsilon^2 h^{(2)}_{2,xxx})}{\widetilde{Ca}}\left[\varepsilon\sin x\left(1+\varepsilon\left(h_2^{(1)}-\sin x\right)+\varepsilon^2 h_2^{(2)}\right)\left(1+\varepsilon\left(h_2^{(1)}-\frac{1}{2}\sin x\right)+\varepsilon^2 h_2^{(2)}\right)\right],
\end{aligned} \tag{2.2.14}$$

where $Q = Q^{(0)} + \varepsilon Q^{(1)} + \varepsilon^2 Q^{(2)} + O(\varepsilon^3)$. Collecting terms of the same order, the leading order $O(1)$ simply states that $Q^{(0)} = 1$, and then at order $O(\varepsilon)$ we obtain

$$Q^{(1)} = h_2^{(1)} + \frac{1}{3\widetilde{Ca}} h^{(1)}_{2,xxx} - \sin x. \tag{2.2.15}$$

This third order linear ODE has an analytic solution given by

$$\begin{aligned}
h_2^{(1)} = Q^{(1)} &+ A_1 \exp\left(-\frac{x}{C^{1/3}}\right) + A_2 \exp\left(\frac{x}{2C^{1/3}}\right)\cos\left(\frac{\sqrt{3}x}{2C^{1/3}}\right) \\
&+ A_3 \exp\left(\frac{x}{2C^{1/3}}\right)\sin\left(\frac{\sqrt{3}x}{2C^{1/3}}\right) + \frac{C\cos x + \sin x}{C^2+1},
\end{aligned} \tag{2.2.16}$$

where $C \equiv \frac{1}{3\widetilde{Ca}}$, and A_1, A_2, and A_3 are unknown constants. For convenience, $Q^{(1)}$ is set to zero by arbitrarily setting $Q \equiv 1$. Note that Q corresponds to the rate of mucus production by the snail.

2.2.5 Boundary conditions

The real challenge lies in identifying the three independent boundary conditions required to solve for A_1, A_2, and A_3. As a logical starting point, we proceed by applying

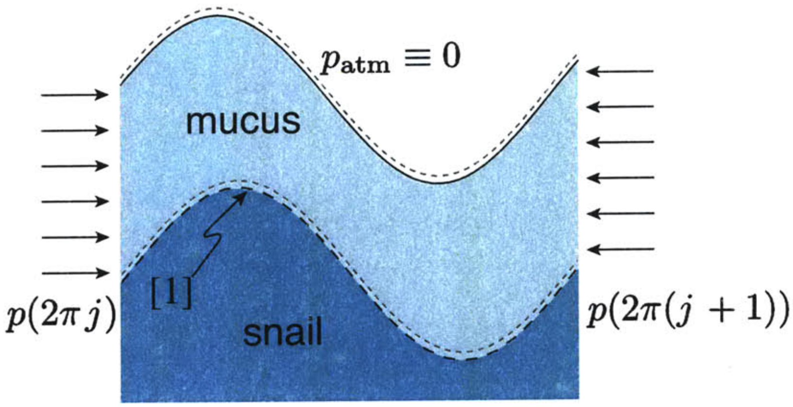

Figure 2.2.2: Free body diagram of a perfectly periodic mucus layer over one wavelength between nodes j and $j+1$. Pressures at these nodes, $p(2\pi j)$ and $p(2\pi(j+1))$, as well as the heights, $h_2(2\pi j)$ and $h_2(2\pi(j+1))$, are equal by the periodic boundary conditions. Above the mucus layer is open to atmosphere with p_{atm} set to zero.

periodic boundary conditions over each wavelength:

$$h_{2,x}(2\pi j) = h_{2,x}(2\pi(j+1)), \tag{2.2.17a}$$

$$h_{2,xx}(2\pi j) = h_{2,xx}(2\pi(j+1)), \tag{2.2.17b}$$

$$h_{2,xxx}(2\pi j) = h_{2,xxx}(2\pi(j+1)), \tag{2.2.17c}$$

where j ranges from 0 to $n-1$. In this limit, A_1, A_2, and A_3 vanish, and these boundary conditions yield no motion of the snail, regardless of the value of $\widetilde{Ca}$. Conducting a force balance on the mucus layer over one wavelength (as shown in Fig. 2.2.2) offers a simple explanation for this result: the periodic boundary conditions ensure that the pressure forces acting on the side control surfaces of the mucus layer precisely cancel. Since the top control surface of the mucus is exposed to ambient air pressure, there can be no net force that acts on the bottom control surface. Thus, no equal and opposite force acts on the snail foot ([1] in Fig. 2.2.2), suggesting that no net propulsive force is generated under strictly periodic boundary conditions.

Instead, the three boundary conditions should be selected by the physical constraints on snail locomotion. Since the moving gastropod is force- and torque-free, the first two conditions should naturally be

$$\Sigma F_y = 0, \tag{2.2.18a}$$

$$\Sigma \tau = 0, \tag{2.2.18b}$$

where F_y refers to forces in the y-direction while τ is a torque in the z-direction. In all generality, the sum of all forces and torques acting on the snail must vanish at low Reynolds number; the forces and torques from the thin film of mucus must therefore balance the forces and torques generated by the external flow around the body and those arising from gravity. For this analysis, we assume the snail does not rotate, and that its shape is sufficiently symmetric that the external viscous torques and y-force vanish. We also assume the organism to be neutrally-buoyant and homogeneous, so the forces and torques due to gravity are zero. As a result, Eqs. (2.2.18a) and (2.2.18b) only require the y-force and z-torque arising from the thin film to vanish.

The final boundary condition arises from consideration of the matching between the internal and the external flow around the organism. By symmetry, we expect the swimming speed of the snail to be of order $V_s \sim \varepsilon^2$. Since we are in the Stokes regime, pressure differences across the moving gastropod should scale linearly with the free stream velocity, and occur at order ε^2 as well. Thus, the pressure difference between the front and back of the snail is zero at $O(\varepsilon)$, the order of our formulation, and the third boundary condition becomes:

$$p(0) = p(2n\pi). \tag{2.2.19}$$

These three boundary conditions allow one to obtain a complete expression for $h_2^{(1)}$ and subsequently solve for the dimensionless propulsive force, F_{prop} at $O(\varepsilon^2)$:

$$\begin{aligned} F_{\text{prop}} &= \int_0^{2n\pi} \left[p\frac{dh_1}{dx} + \frac{\partial u}{\partial y}|_{y=h_1} \right] dx \\ &= 3C \int_0^{2n\pi} \left[-h^{(1)}_{2,xx} \cos x + h^{(1)}_{2,xxx}(h_2^{(1)} - \sin x) + h^{(2)}_{2,xxx} \right] dx. \end{aligned} \tag{2.2.20}$$

Note that the integral of $h^{(2)}_{2,xxx}$ vanishes by the matching pressure boundary condition, which is equivalent to $h_{2,xx}(0) = h_{2,xx}(2n\pi)$. Referring back to the constants in Eq. (2.2.16), A_1, in particular, is a non-trival function of $\widetilde{Ca}$. Hence, unlike the strictly periodic boundary condition case, the expression for $h_2^{(1)}$ now contains a non-periodic function that gives rise to a non-zero propulsive force.

2.2.6 Crawling speed

To balance the thin-film propulsive force, it is necessary to evaluate the external drag $\widehat{F}_{\text{drag}}$ caused by the motion of the snail. For simplicity, the snail is modeled as approximately spherical, with radius $\widehat{R}$. Although approximate, this model yields an order of magnitude approximation for the speed of our model snail. Non-dimensionalizing $\widehat{F}_{\text{drag}}$ by $\mu \widehat{V}_w \widehat{w}$, the right hand side of (2.2.11) becomes $F_{\text{drag}} \approx 6\pi f V_s/\mu^*$, where V_s is the snail speed scaled by $\widehat{V}_w$ and $\mu^* \equiv \mu/\mu_{water}$, the viscosity ratio of mucus to water. A correction factor f accounts for the aspherical shape of the snail as well as the influence of the free surface on the drag coefficient; for the present analysis, f will be treated as known for a given crawler. By combining this scaling with the $O(\varepsilon^2)$ term in the force on the foot generated by the mucus layer, the following expression for V_s is obtained:

$$V_s \approx \frac{\varepsilon^2 \mu^*}{af} F_{\text{prop}}(\widetilde{Ca}, n), \tag{2.2.21}$$

where F_{prop}, the total propulsive force function, is plotted in Fig. 2.2.3(a) for different values of n. The exact formula for F_{prop} is not reproduced in this paper because it is long and not informative for the purpose of this analysis, but it is straightforward to calculate with symbolic packages. Note that the width of the snail foot, $\widehat{w}$, is taken to be on the same order as $\widehat{R}$; thus, they drop out of Eq. (2.2.21).

2.2.7 Results

Fig. 2.2.3 shows that the propulsive force vanishes in the limits of both large and small surface tension. In the limit of infinitely large surface tension ($\widetilde{Ca} \to 0$), the interface between air and mucus is undeformable and so is analogous to a flat surface

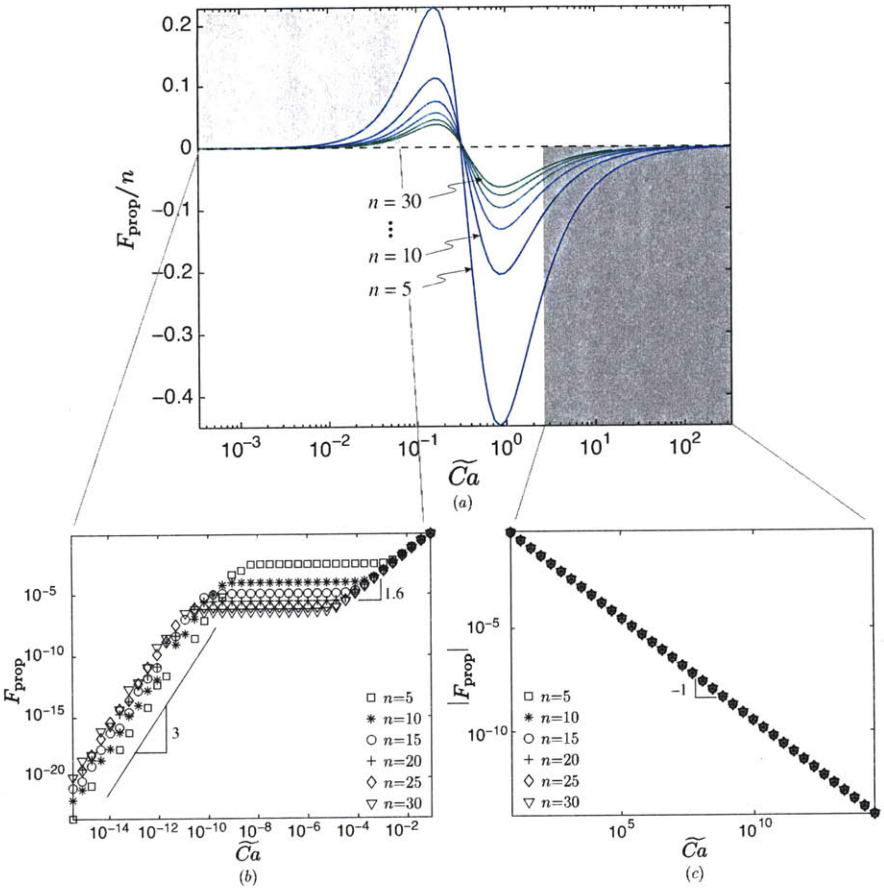

Figure 2.2.3: (a) Dimensionless propulsive force, F_{prop}, normalized by the number of wavelengths, n, as a function of the modified capillary number, $\widetilde{Ca} \equiv \mu \widehat{V}_w / a^3 \sigma$, where the values of n range from 5 to 30 in increments of 5. In (b) and (c), the absolute value of the dimensionless force, F_{prop}, is plotted on a logarithmic scale to show the power-law decay in the limits of $\widetilde{Ca} \to 0$ and $\widetilde{Ca} \to \infty$ respectively. The propulsive force exhibits a $\widetilde{Ca}^{-1}$ decay for large $\widetilde{Ca}$, while it decays as $\widetilde{Ca}^{3}$ for small $\widetilde{Ca}$.

that cannot sustain shear stress. A snail would simply slip on such surfaces. The detailed behavior for small values of $\widetilde{Ca}$ is shown in Fig. 2.2.3(b). The dimensionless force follows the power-law decay $F_{\mathrm{prop}} \sim \widetilde{Ca}^{3}$ for decreasing $\widetilde{Ca}$ for all values of n.

With zero surface tension ($\widetilde{Ca} \to \infty$), a pressure difference across the interface cannot be sustained and so cannot drive the flow within the mucus; hence no propulsive force can be generated in this low surface tension limit either. In this case, the force follows for all n the power-law decay $|F_{\mathrm{prop}}| \sim \widetilde{Ca}^{-1}$ as shown in Fig. 2.2.3(c).

Note that the propulsive force goes from positive to negative at a moderate value

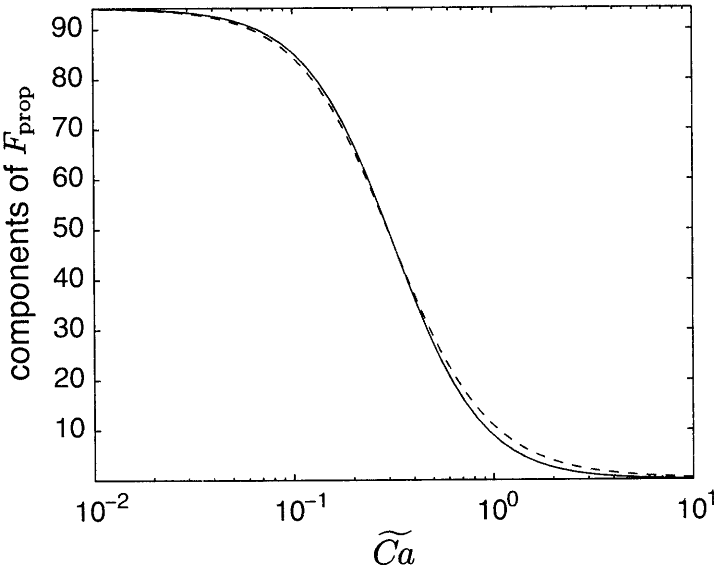

Figure 2.2.4: Absolute magnitudes of components of dimensionless propulsive force due to pressure (solid line) and due to shear (dashed line) as a function of $\widetilde{Ca}$ for $n = 10$. (note that the shear force is negative). Hence, the total propulsive force which is the sum of these two forces is non-zero only when there is a difference between the two.

of $\widetilde{Ca}$ that, in the case of $n = 10$, is around 0.3. Physically, this implies that the snail switches from retrograde waves to direct waves at this critical $\widetilde{Ca}$. In addition, Fig. 2.2.3(a) shows that the propulsive force exhibits two distinct maxima for retrograde and direct waves, at values of $\widetilde{Ca}$ corresponding to 0.15 and 0.8, respectively. Since the maximum propulsive force for the direct waves is higher than that for the retrograde, the direct waves may be a faster mode of locomotion for water snails. This points to a possible biological advantage of direct over retrograde waves.

Fig. 2.2.4 quantifies the components of propulsive force due to pressure and shear. It is important to note that the force due to shear (dashed line) is negative. In the low $\widetilde{Ca}$ limit, these two components precisely cancel, leading to no motion. When $\widetilde{Ca}$ is high, they both vanish. For intermediate values of $\widetilde{Ca}$, a difference in the magnitudes of these forces results in a net propulsive force. Note the existence of a finite value of $\widetilde{Ca}$ for which the propulsive force reaches zero.

Going back to the dynamic boundary condition Eq. (2.2.7), one can calculate the pressure and shear stress distribution to $O(\varepsilon)$ inside the mucus layer. These are

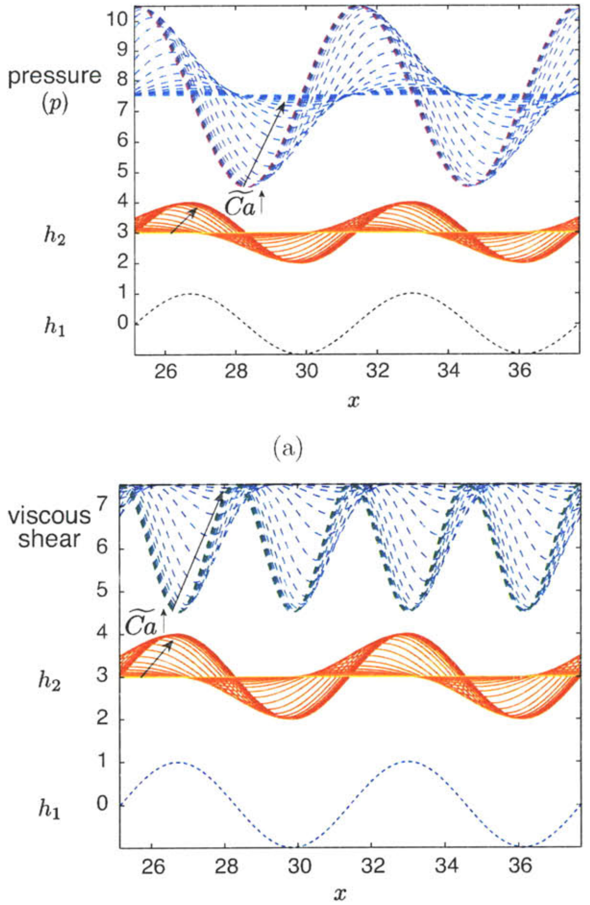

(a)

(b)

Figure 2.2.5: Dimensionless pressure (a, dashed line) and shear stress (b, dashed line) within the mucus over two wavelengths for $n = 10$. The single dotted line in both (a) and (b) is the shape of the foot, h_1 while the solid lines describe the shape of the interface, h_2 for different values of $\widetilde{Ca}$. Black arrows indicate the direction of increasing $\widetilde{Ca}$.

plotted in Figure 2.2.5 for $n = 10$ along with the shape of the interface, $h_2^{(1)}$. In the large $\widetilde{Ca}$ limit, the interface shape exactly conforms to the shape of the foot h_1; in the small $\widetilde{Ca}$ limit, the interface becomes flat. At intermediate $\widetilde{Ca}$, there exists an asymmetry in the interface shape, associated with the exponential term in Eq. (2.2.16), that gives rise to the non-trivial propulsive force. The interface shape, pressure and shear stresses are plotted for the first wavelength and the last (corresponding to the front and end of the snail) for $n = 10$ in Fig. 2.2.6. As shown in this figure, the mucus thickness at the ends deviates substantially from extrapolated

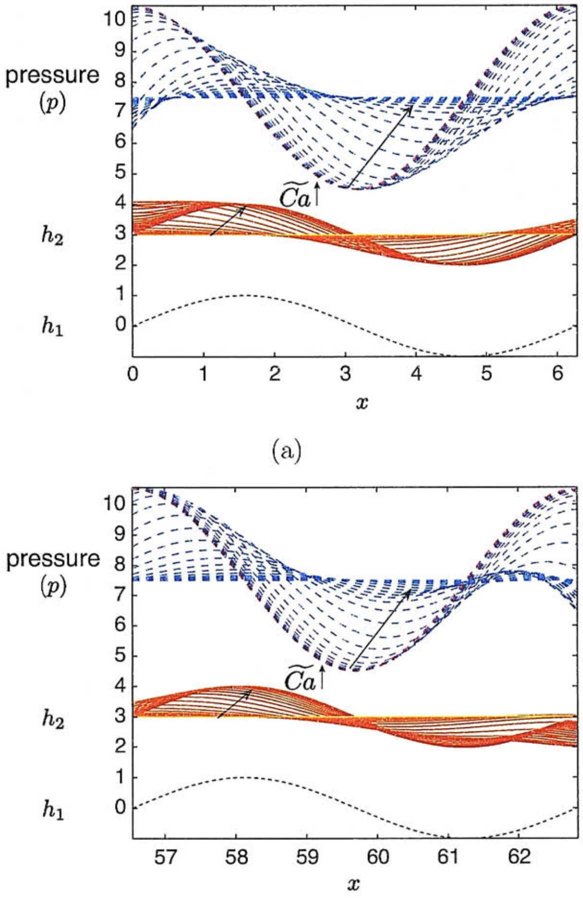

(a)

(b)

Figure 2.2.6: Dimensionless pressure (dashed line) and the interface shape (solid line) in the front (a) and end (b) of the snail for $n = 10$. The dotted line is the shape of the foot, and black arrows are in the direction of decreasing surface tension.

periodic values creating an asymmetry between the head and the tail. Thus, although the pressures at the ends of the crawler are equal at $O(\varepsilon)$, there exists a net $O(\varepsilon^2)$ pressure force acting on the side control surfaces, owing to the a $O(\varepsilon)$ difference in thickness of the mucus layer (see Fig. 2.2.7). To balance this net force, there has to be a force acting on the bottom surface of the mucus layer; thus, there exists an equal and opposite force acting on the foot of the snail, corresponding to the propulsive force.

As suggested by Fig. 2.2.3, surface tension is the essential ingredient in this mode of locomotion, and the propulsive force vanishes in both limits of asymptotically small (large $\widetilde{Ca}$) and large (small $\widetilde{Ca}$) surface tension. The snail would therefore have to

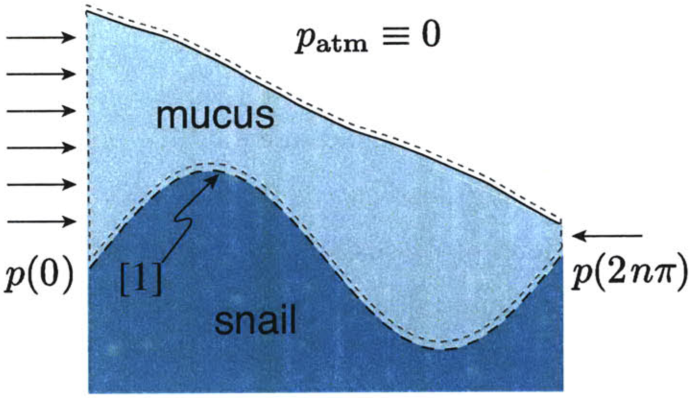

Figure 2.2.7: Free body diagram of an asymmetric mucus layer across the foot of the snail. (For simplicity, $n = 1$ in this diagram.) Pressures at the ends, $p(0)$ and $p(2n\pi)$ are equal by the boundary condition; however, they act over two different mucus thicknesses, resulting in a net pressure force.

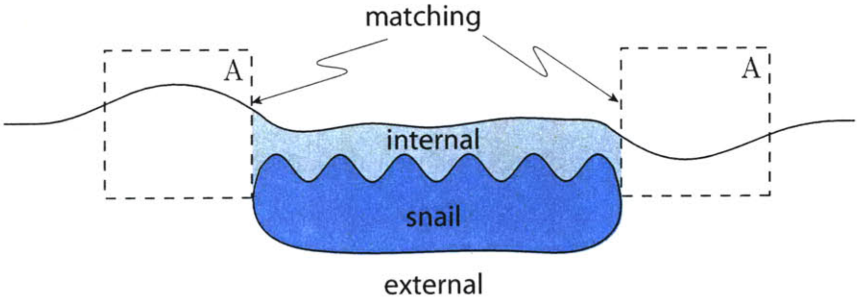

Figure 2.2.8: Schematic of the snail with three distinct flow regions. The layer of mucus above the snail foot is denoted as 'internal' while the ambient flow around the snail's body is 'external.' The two dashed boxes (labeled A) enclose the matching regions that connect the internal and external flows.

tune the way it deforms its foot to exploit the property of the fluid-air interface. As the foot is deformed, it forces a lubrication flow in the mucus layer above which leads to the deformation of the free surface. The resulting topography of the free surface, regularized by surface tension, is then exploited by the organism to generate a propulsive force.

2.2.8 Matching internal and external flows

In our analysis, we have neglected the fluid forces on the organism, $\mathbf{F}_{\text{match}}$, arising from the intermediate matching region between the internal (mucus) and the external flows. Since the propulsive force of the snail mostly arises from the asymmetric shape of the free surface at the head and tail of the foot, this requires further comment.

Physically, since we are calculating the internal and external flows separately, both need to be considered. In order to first estimate the magnitude of $\mathbf{F}_{\text{match}}$ due to the external flow, we refer to the work by Berdan and Leal [9] who studied the motion of a sphere near a deformable fluid-fluid interface. As an extension of previous work in which the interface is assumed to be flat [40, 41], the work in Ref. [9] considers the limit of small interfacial deformation and its effects on the translating body. Unlike our current analysis, the velocity of the sphere is not governed by the shape of the free surface but is fixed as $\widehat{U}$. The small parameter in this paper, $\hat{\epsilon}$, reduces to a capillary number, $\hat{\epsilon} = \mu\widehat{U}/\sigma$, when gravitational effects are not included. Berdan and Leal showed that in the case of a sphere moving parallel to the free surface, the deformation of the interface only has a vertical force contribution at $O(\hat{\epsilon})$. In the current analysis, $\mathbf{F}_{\text{int}}$ and $\mathbf{F}_{\text{ext}}$, the forces considered in Eq. (2.2.10), are of $O(\varepsilon^2)$. Therefore, in order to neglect $\mathbf{F}_{\text{match}}$ consistently, the following condition has to be satisfied:

$$\hat{\epsilon}^2 \ll \varepsilon^2, \tag{2.2.22}$$

which requires one to have a look at how $\hat{\epsilon}$ and ε are defined. Since $\widehat{U}$ is $\widehat{V}_s$ in our problem, we have $\hat{\epsilon} \sim \mu\widehat{V}_s/\sigma$. Recalling from §2.2.3, the capillary number, Ca, is defined in terms of the wave velocity, $\widehat{V}_w$. Because it has been shown that $V_s = \widehat{V}_s/\widehat{V}_w$ scales as ε^2, $\hat{\epsilon}$ can be expressed as

$$\hat{\epsilon} \equiv \frac{\mu\widehat{V}_s}{\sigma} \sim \varepsilon^2\frac{\mu\widehat{V}_w}{\sigma} \equiv \varepsilon^2\text{Ca}. \tag{2.2.23}$$

When one replaces Ca with $a^3\widetilde{Ca}$ and rearranges the terms, the criterion to neglect

$\mathbf{F}_{\mathrm{match}}$ in Eq. (2.2.22) reduces to

$$\varepsilon^2 a^6 \widetilde{Ca}^2 \ll 1. \tag{2.2.24}$$

Since a and ε are both small parameters asymptotically approaching zero in the lubrication analysis in the limit of small deformation amplitude, $\varepsilon^2 a^6 \ll 1$, Eq. (2.2.24) represents a weak constraint on the validity of neglecting forces from the intermediate region.

The second matching force to consider is that induced by the internal flow. Since there is, in general, a height difference between the mucus at the front and the back of the snail, the fluid surface will be distorted at either end to match with the flat surface far away. Our work will therefore be valid in the limit where the capillary forces resulting from these distortions can be neglected, corresponding to an asymptotic limit which we now characterize.

The two relevant length scales to consider for matching the distorted fluid interface to the flat free-surface in the far-field are the capillary length, $\hat{\ell}_c \sim \sqrt{\sigma/\rho g}$ (ρ is the fluid density), and the width of the snail, $\hat{w}$.The fluid interface will be distorted over a length, $\hat{\ell}$, into the fluid, where $\hat{\ell} \sim \min(\hat{\ell}_c, \hat{w})$. The typical curvature pressure arising from surface distortion will be on the order of $\sim \sigma\delta\hat{h}/\hat{\ell}^2$, acting on typical height difference $\delta\hat{h}$ between the free surface near the snail and the far-field height of the free surface, and therefore contributes to a force on the snail (per unit width) on the order of $\sim \sigma(\delta\hat{h})^2/\hat{\ell}^2$. Since $\delta\hat{h} \sim \varepsilon\hat{H} \sim \varepsilon a\hat{\lambda}$, the capillary force is on the order of $\sim \sigma\varepsilon^2 a^2\hat{\lambda}^2/\hat{\ell}^2$. This force has to be compared with that arising from the external flow, given by $\hat{p}_{ext}\hat{R}$ (again, per unit width) where $\hat{p}_{ext}$ is the typical magnitude of the pressure outside the organism as it is crawling. Since $\hat{p}_{ext} \sim \mu\hat{V}_s/\hat{R}$ we have $\hat{p}_{ext}\hat{R} \sim \mu\hat{V}_s \sim \varepsilon^2\mu\hat{V}_w$. The matching condition becomes therefore $\sigma\varepsilon^2 a^2\hat{\lambda}^2/\hat{\ell}^2 \ll \varepsilon^2\mu\hat{V}_w$, which is equivalent to

$$\hat{R}^2/\hat{\ell}^2 \ll a\,\widetilde{Ca}\,n^2, \tag{2.2.25}$$

where we have used the estimate $\hat{R} \sim n\lambda$. The second matching condition, Eq. (2.2.25), requires that the number of wavelengths along the snail's foot, n, be sufficiently large.

2.3 Discussion

Here, we have presented a simplified model of water snail locomotion. The physical picture that emerges is the following: the undulation of the snail foot causes normal stresses that deform the interface and drive a lubrication flow. The resulting stress distribution couples to the topography of the snail foot, leading to a propulsive force. This force vanishes in the limit of $\widetilde{Ca} \to 0$, where the interface is flat, and of $\widetilde{Ca} \to \infty$, where the topographies of the interface and the snail foot precisely match. A finite propulsive force is obtained for intermediate values of $\widetilde{Ca}$. This interplay between the free surface and the snail foot distinguishes water snail locomotion from that of their terrestrial counterparts. For the latter, the solid substrate on which the snail crawls is fixed; hence, the shape of the snail foot alone determines the pressure and shear stresses generated within the mucus layer. For water snails, however, the interface is deformed due to the flow created in the mucus by the foot undulation; the interface, in turn, affects the dynamics within the mucus layer, creating pressure and shear stresses that act on the foot. This nonlinear coupling between the foot geometry, surface tension, and dynamics within the mucus layer makes the water snail crawling strategy a less straightforward mode of locomotion.

A direct analogy exists between the thin film comprising the mucus layer of water snails and those arising in coating flows; for example, those used in photolithographic processes to fabricate various electronic components. This class of fluids problem has been well studied, both experimentally [65, 66, 52] and theoretically [65, 66, 54, 55, 60, 58, 28], an example of which includes spin coating. Kalliadasis *et al.* [35] used lubrication theory to show that in the limit of small Ca, the interfacial features become less steep, an effect also captured by our model. Mazouchi and Homsy [46] demonstrated that, for large capillary number, the shape of the free surface nearly follows the topography. In the context of water snail locomotion, we saw in §2.2.4 that the free surface conforms to the shape of the foot in the same limit.

Our study is only the first step towards a quantitative understanding of gastropod crawling beneath free surfaces. It is significant in that we have demonstrated the plausibility of locomotion with the minimal ingredients: Newtonian fluids and small amplitude deformations. Nevertheless, outstanding issues remain. In the case of adhesive snail locomotion on land, the non-Newtonian properties of snail mucus, such as a finite yield stress and finite elasticity, play an essential role [23]. Non-Newtonian mucus is likewise expected to have a significant effect for water snails. Furthermore, there need to be more systematic observational studies to identify which water snail species exhibit which modes of "inverted crawling". As reported by Copeland [19, 20] and Deliagina and Orlovsky [22], some species of water snails rely entirely on cilia for propulsion beneath the free surface. If such ciliary motion results in no free surface deformation, the physical mechanism examined in this paper is of little relevance, and a closer look at the cilia-induced flow is suggested. Alternatively, the non-Newtonian properties of the mucus may prove to be significant in this case. Categorizing different species according to their propulsion mechanism of crawling (i.e. cilia versus muscle contraction) and the constitutive properties of their mucus would provide a more complete physical picture of this intriguing form of locomotion.

Chapter 3

Point Swimmer

We are now interested in a general description of low Reynolds swimmers that use a free surface to move forward. While answering questions about a specific organism, the preceding analysis of the motion of water snails contains restrictions that prevent generalization to other types of swimmers that take advantage of the free surface. For instance, the foot of the water snail is assumed to be very close to the free surface, separated only by a thin layer of mucus. In addition, in order to linearize the problem, we only considered asymptotically small free surface deformations. In this chapter, we discuss a new description of the low Reynolds swimmer that no longer contains these geometrical constraints. Instead, the only mathematical simplifications are to consider a two-dimensional swimmer and to model it as a "point".

A two-dimesional description of our swimmer is feasible because the well-known Stokes Paradox does not apply to self-propelling bodies in a Stokes flow. The paradox is that the motion of a cylinder in a viscous fluid yields a finite fluid velocity in the far-field and is, therefore, not physically realistic. G.I. Taylor discussed the difference between a cylinder moving in a viscous fluid and a $2D$ self-propelling body [68]. He showed that unlike the cylinder, the influence of the motion of the self-propelling organism extends only a short distance from the body and, therefore, quiescent boundary conditions at infinity can be satisfied. In mathematical terms, this implies that the cylinder consists of logarithmic singularities that do not decay in the far-field, while the self-propelling body contains only higher order singularities since it is force-free. In the following analysis, our swimmer is modeled as a sum of a force-dipole, or a stresslet, and other higher order poles.

Modeling the low Re swimmer as a point singularity is not a new concept. In particular, the stresslet singularity has been widely used to model the collective behavior of swimming microorganisms [51, 62, 31, 59]. Interestingly, the sign of the stresslet strength has important physical implications. When the stresslet is less than zero, the microorganism (termed a "pusher") swims using its tail. If the strength is positive, the swimmer pulls on the surrounding fluid in some fashion to move forward and is accordingly called a "puller". This distinction manifests itself in the large-scale behavior of swimmers: pushers align themselves with the local flow and facilitate mixing, while pullers act to dissipate disturbances [59].

This singularity description of our swimmer is consistent with the spirit of our analysis in that we are no longer interested in a specific organism, or the geometrical details of the swimmer's motion. Instead, our focus is on the far-field flows for a given free surface shape and the role of the free surface in propulsion of the swimmer.

3.1 Conformal map

Our analysis is restricted to two-dimensions as it relies heavily on the use of conformal mapping techniques. In simple terms, a conformal map locally stretches and rotates a given two-dimensional domain into a simpler one while preserving the angle between any pair of intersecting curves. The advantage of using this map is that all of the geometrical complexity of a given problem gets "absorbed" in this map, rendering the exact mathematical analysis of complicated geometries more tracktable [6]. The single most important theorem regarding conformal mapping may be Riemann's Theorem which guarantees the existence of conformal transformations between any two *simply connected* contours [15]. The real challenge then lies in identifying such a map for a given system. Unfortunately, there exists no clear guideline for finding conformal maps, apart from one's intuition, experience, and, in many cases, a bit of good fortune.

In recent years, this mathematical technique is finding its place in applied sciences, especially in interfacial dynamics which often consist of time-dependent free moving boundaries, such as viscous fingering and solidification [6]. In addition, conformal mapping is being applied to other two-dimensional problems in material sciences, examples of which include brittle fracture and viscous sintering, as well as stochastic problems, such as diffusion-limited aggregation. One particular application of the conformal map that is of significance to us is the work by Jeong and Moffatt [33]. In their seminal paper, they modeled the flow generated by two counter-rotating cylinders beneath a free surface in the low Reynolds limit as a single potential dipole placed on the axis of symmetry. This flow results in symmetric deformations of the free surface above, which were calculated for a given dipole strength and fluid properties using the conformal map methods. It is noteworthy that the conformal map approach to this physical system allowed them to produce *exact* solutions for large nonlinear deformations of the free surface. Furthermore, their analytic results exhibit remarkable agreement with the experimental data of free surface deformations for different rotation rates of the cylinders.

Inspired by this work, we similarly use a conformal map to solve for the shapes of a free surface regularized by surface tension. The flow that leads to the surface deformation is generated by the "squirming" [43, 12] of the swimmer that undergoes a steady translation underneath the free surface. As previously discussed, the swimmer's motion is represented by a linear combination of singularities, such as a stresslet, potential dipole and quadrupole. This seemingly minor point sets our work apart from that of Jeong and Moffatt in that we are able to find a class of generalized exact solutions even upon the inclusion of a rotational stresslet singularity. In addition, our problem includes asymmetric deformations, requiring multiple parameters to describe the shape of the interface. Jeong and Moffatt fixed the dipole strength and solved for a shape parameter that uniquely defines a free surface shape for a given dipole strength. In our case, we have multiple singularities that describe the swimmer's motion and more than one parameter that determines the free surface shape. Another complication comes from the fact that only certain combinations of singularities lead to a steady motion of the swimmer and a fixed free surface shape translating with it; this combination is not known *a priori*. In order to circumvent these difficulties, we approach our problem in the inverse manner from Jeong and Moffatt. Namely, we fix the swimmer's steady state velocity and the interfacial shape as input and solve for the corresponding singularity types and strengths that satisfy the given steady state condition.

Another difference between these two systems is that in the flow generated by the counter-rotating cylinders, the amount of power one can put in is essentially unlimited and is only restricted by the experimental setup. In our system, however, the power is generated by the swimmer itself, which, in biological systems, is often motivated to preserve energy. We focus on this very point in Chapter 4 and study the free surface shapes that result in the most energetically favorable motion. The current chapter then consists of the derivation of exact solutions for our model problem.

3.2 Governing equations — complex variables

In the incompressible Stokes regime where inertia is negligible, the Navier-Stokes equations may be written in terms of a streamfunction $\hat{\psi}$ that satisfies the following biharmonic equation

$$\nabla^4 \hat{\psi}(\hat{x}, \hat{y}) = 0. \tag{3.2.1}$$

Introducing the complex-valued coordinate $\hat{z} = \hat{x} + \mathrm{i}\hat{y}$, the solution to this biharmonic equation takes the form of

$$\hat{\psi} = \mathrm{Im}[\bar{\hat{z}} \hat{f}(\hat{z}) + \hat{g}(\hat{z})]. \tag{3.2.2}$$

Referred to as *Goursat functions* [15], $\hat{f} \equiv \hat{f}(\hat{z})$ and $\hat{g} \equiv \hat{g}(\hat{z})$ are analytic functions of $\hat{z}$ inside the fluid region except at isolated points where singularities are deliberately introduced.

All the physical variables that describe a flow [36] can be expressed in terms of these two functions:

$$\begin{aligned}\frac{\hat{p}}{\mu} - \mathrm{i}\hat{\omega} &= 4\hat{f}'(\hat{z}),\\ \hat{u} + \mathrm{i}\hat{v} &= -\hat{f}(\hat{z}) + \hat{z}\overline{\hat{f}'(\hat{z})} + \overline{\hat{g}'(\hat{z})},\\ \hat{e}_{11} + \mathrm{i}\hat{e}_{12} &= \hat{z}\overline{\hat{f}''(\hat{z})} + \overline{\hat{g}''(\hat{z})},\end{aligned} \tag{3.2.3}$$

where $\hat{p}$ is the fluid pressure with μ as the dynamic fluid viscosity, $\hat{\omega}$ is the vorticity, $(\hat{u}, \hat{v})$ is the fluid velocity, and $\hat{e}_{ij}$ is the fluid rate-of-strain tensor. Primes denote differentiation with respect to $\hat{z}$, overbars denote complex conjugates, and hats indicate dimensional variables.

In our model problem, the two-dimesional fluid domain is bounded by an air-water interface, δD, regularized by surface tension, σ. On this interface, we apply the usual stress boundary condition balancing the pressure jump and viscous stresses with the free surface curvature:

$$-\hat{p}n_i + 2\mu\hat{e}_{ij}n_j = \sigma\hat{\kappa}n_i, \tag{3.2.4}$$

where $\hat{\kappa}$ is the surface curvature, and n_i is the outward unit vector normal to the interface.

All the variables in our problem are non-dimensionalized as follows:

$$\begin{gathered}\hat{z} = \hat{h}z, \quad \hat{z}_d = \hat{h}z_d, \quad \hat{u} + i\hat{v} = \hat{U}(u + iv), \quad \hat{\psi} = \hat{U}\hat{h}\psi,\\ \hat{f} = \hat{U}f, \quad \hat{g} = \hat{U}\hat{h}g, \quad \hat{p} = \frac{\mu\hat{U}}{\hat{h}}p,\end{gathered} \tag{3.2.5}$$

where $\hat{z}_d$ is the dimensional location of the swimmer, $\hat{h}$ is the magnitude of $\hat{z}_d$ or the vertical distance of the swimmer from the interface, and $\hat{U}$ is a characteristic speed of translation. Going back to the stress boundary condition, the dimensionless form Eq. (3.2.4) is equivalent to

$$\frac{dH}{ds} = -\frac{\mathrm{i}}{2\mathrm{Ca}}\frac{d^2z}{ds^2}, \tag{3.2.6}$$

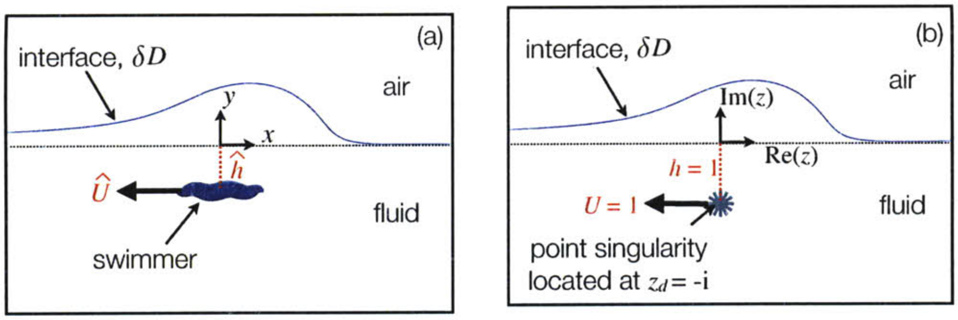

Figure 3.3.1: The idea of the singularity model: a finite-body swimmer beneath a free surface is modelled as a point stresslet singularity.

where ds is a differential element of arc length along the free surface and

$$H \equiv f(z) + z\overline{f}'(\overline{z}) + \overline{g}'(\overline{z}). \tag{3.2.7}$$

Hence, after integrating once with respect to s, Eq. (3.2.6) becomes

$$f(z,t) + z\overline{f}'(\overline{z}) + \overline{g}'(\overline{z}) = -\frac{\mathrm{i}}{2\mathrm{Ca}}\frac{dz}{ds}. \tag{3.2.8}$$

Note that one important dimensionless number that comes out of this non-dimensionlization is the capillary number Ca, which reflects the ratio of viscous to surface tension effects,

$$\mathrm{Ca} = \frac{\mu\hat{U}}{\sigma}. \tag{3.2.9}$$

3.3 The swimmer — singularity description

As briefly discussed, the Goursat functions $f(z)$ and $g(z)$ are analytic everywhere inside the fluid domain, except at specific singular locations. In our problem, $f(z)$ and $g(z)$ contain singularities at the swimmer location, z_d (as illustrated in Figure 3.3.1), and the type and strength of these singularities determine the effective "squirming" motion of the swimmer. Since all the physical variables are written in terms of these two functions (see Eq. (3.2.3)), one can easily see that the choice of a particular singularty has an immediate effect on the flow as well as the shape of the interface.

For instance, inclusion of a *logarithmic* singularity of $f(z)$ corresponds to a *stokeslet*, or point force singularity, which is not allowed in order to ensure that the swimmer exerts no net force on the flow. Instead, we take the next order singularity, and $f(z)$ is allowed to have a simple pole at z_d (the derivative of the logarithm),

$$f(z) = \frac{s^*}{z - z_d} + \text{analytic}. \tag{3.3.1}$$

Then in order to ensure that the resultant velocity field decays as $1/|z - z_d|$, not $1/|z - z_d|^2$, we must also have

$$g'(z) = \frac{s^* \overline{z_d}}{(z - z_d)^2} + \text{analytic}. \tag{3.3.2}$$

This combination of singularities in $f(z)$ and $g'(z)$ is known as a *stresslet* of strength s^* at z_d. Similarly, inclusion of a logarithmic singularity of $g(z)$ is not allowed since it leads to a net torque on the fluid, violating the torque-free condition of the swimmer.

In order to understand the physical implication of a stresslet, we revisit the difference between a passive object (i.e. a cylinder) and a self-propelling body both moving at a constant speed in Stokes flow in more detail. In both cases, the net force acting on the body must sum to zero; however, the resultant flow fields around each body are very different. In the case of a cylinder, the forces around it account for both the viscous drag from the fluid and an external force pulling the body, represented as a stokelet. On the other hand, the self-propelling swimmer only has viscous forces acting on the body, leaving no clear distinction between the drag versus propulsive forces. To better distinguish the two, one may imagine a sperm whose oscillating tail provides a net forward force and whose head experiences an equal and opposite force of drag. These two separate forces may be modeled as stokeslets, and as they are brought infinitesimally close together, they resemble a force-dipole, or a stresslet.

Going back to our mathematical formulation of the swimmer, there are two important points to consider. First, we allow $g'(z)$ to have other higher order poles at z_d, while limiting the singularty of $f(z)$ to be a simple pole. This degree of freedom is necessary to ensure that the free surface boundary condition is satisfied while yielding a steady state motion of the swimmer. Thus, we seek to discover the nature of the effective potential multipoles that a swimmer must generate in order to swim steadily beneath a free surface. The other important point pertains to the steady state nature of our solution, meaning that the net motion, the free surface shape, and the singularities are all independent of time. Here an important distinction needs to be made between the work by Trouilloud *et al.*[71] and our current model. Trouilloud *et al.* considered reciprocal swimmers subject to the Scallop Theorem [56, 42, 13] by modeling them as stresslets *oscillating in time*. They found that these swimmers rely on temporarily asymmetric free surface deformations to move. These reciprocal swimmers, when averaged over time, yield zero singularities, and their net motion comes strictly from the unsteady nature of the free surface deformation. Thus, we cannot consider our current model as a time-averaged version of that of Trouilloud *et al.* Instead, it is more accurate to imagine our swimmer as an organism that acts on the surrounding fluid only in a completely symmetric fashion *at all times* (i.e., an "imaginary" swimmer with two corkscrews that rotate symmetrically about its head). This implies that the swimmer, modeled as a permanent singularity, would not be able to generate motion in an unbounded fluid. Rather, its motion is enabled by the presence of the free surface and may be enhanced by deformations.

3.4 Swimming beneath free surface — conformal map approach

3.4.1 General solutions

Based on the Riemann mapping theorem, one may find $z(\zeta)$ that maps a unit disc $|\zeta| \leq 1$ to the fluid region beneath the free surface (see Figure 3.4.1). Accounting for a pole due to the free surface extending to infinity (mapped to $\zeta = -\mathrm{i}$), the most general form of this mapping is

$$z(\zeta) = \frac{a}{\zeta + \mathrm{i}} + \sum_{k=0}^{\infty} a_k \zeta^k \tag{3.4.1}$$

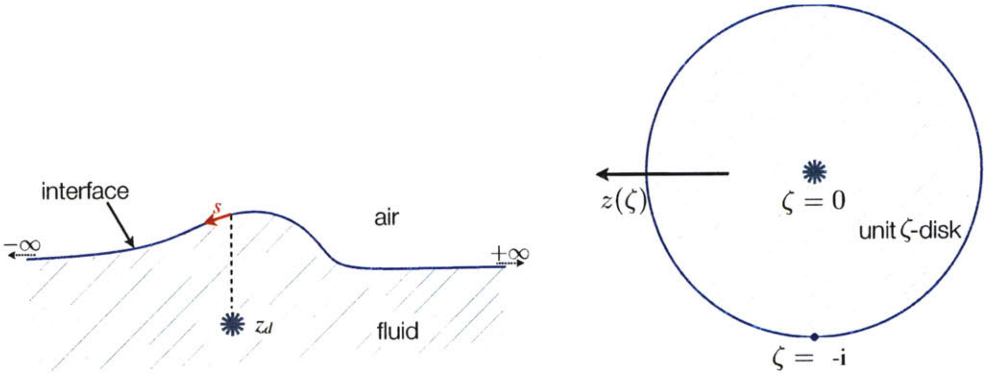

Figure 3.4.1: Conformal mapping $z(\zeta)$ from the unit ζ-disc to the fluid region beneath the interface. In this mapping, $\zeta = 0$ maps to the swimmer at $z = z_d$, and $\zeta = -\mathrm{i}$ maps to the interface at infinity. The variable s denotes the arclength and is defined positive going from positive to negative infinity.

where a and $\{a_k\}$ are complex coefficients. For a one-to-one function, the condition $dz/d\zeta \neq 0$ must hold inside the unit disc. We also prescribe the swimmer's position z_d to be the image of $\zeta = 0$,

$$z_d = z(0). \tag{3.4.2}$$

Moving reference frame and far-field condition

Because we are only concerned with steady state solutions where the swimmer moves at a constant velocity and the free surface shape relative to the swimmer is fixed, we move to the co-travelling frame of the swimmer in which the swimmer and the shape of the free surface are both stationary. In this reference frame, the kinematic condition on the interface becomes

$$\mathbf{u} \cdot \mathbf{n} = 0. \tag{3.4.3}$$

If the normal vector $\mathbf{n} = (n_x, n_y)$, the complex normal $n_x + \mathrm{i}n_y$ is $-\mathrm{i}dz/ds$, where s increases along the interface from positive infinity to negative (see Figure 3.4.1).

Using this fact, Eq. (3.4.3) can be expressed in complex form as

$$\mathrm{Re}\left[(u+\mathrm{i}v)\mathrm{i}\frac{d\bar{z}}{ds}\right]=0. \tag{3.4.4}$$

Then by combining the stress boundary condition (3.2.8) with this kinematic boundary condition (3.4.4), the following must hold on the interface

$$\bar{z}f(z)+g(z)=0, \tag{3.4.5}$$

which is equivalent to the interface being a streamline in physical terms. Note that this expression provides a simple relationship between the two Goursat functions to be re-visted in our analysis. In addition, assuming the swimmer moves at $U=-1$ (in the *negative* horizontal direction) implies a unit far-field velocity. As $z\to\infty$, $f(z)$ and $g(z)$ are given by

$$f(z)\to f_\infty+\frac{f_\infty^{(1)}}{z}+\ldots \qquad \text{and} \qquad g'(z)\to g_\infty+\frac{g_\infty^{(1)}}{z}+\ldots, \tag{3.4.6}$$

and recalling the definition of the velocity field in terms of $f(z)$ and $g(z)$,

$$u+\mathrm{i}v\to -f_\infty+\overline{g_\infty}+\mathcal{O}(|z|^{-1}). \tag{3.4.7}$$

Then, as a consequence of the moving reference frame, it follows that

$$-f_\infty+\overline{g_\infty}=1. \tag{3.4.8}$$

After some manipulation using equations (3.2.8), (3.4.5), and (3.4.8) (as shown in Appendix A.1), we obtain

$$f_\infty=-\frac{1}{2}+\frac{\mathrm{i}}{4\mathrm{Ca}} \qquad \text{and} \qquad g_\infty=\frac{1}{2}-\frac{\mathrm{i}}{4\mathrm{Ca}}. \tag{3.4.9}$$

Solving in the ζ-plane

As mentioned previously, the advantage of the conformal mapping method is the ability to solve a given problem in a much simpler geometry, in this case, a unit circle. In order to do so, we now introduce the counterparts to the Goursat functions, $f(z)$ and $g(z)$, in this new domain:

$$F(\zeta) \equiv f(z(\zeta)), \quad G(\zeta) \equiv g(z(\zeta)). \tag{3.4.10}$$

It is important to note that, as $f(z)$ has a simple pole at the position of the swimmer, the Goursat function $F(\zeta)$ must have a simple pole at $\zeta = 0$. Therefore, $F(\zeta)$ takes the form of

$$F(\zeta) = \frac{F_d}{\zeta} + F_0 + \mathcal{O}(\zeta) \tag{3.4.11}$$

for some constant F_d to be determined later. Recognizing that the kinematic condition (3.4.3) on the boundary can be written as

$$\mathrm{Re}\left[2fi\overline{\left(\frac{dz}{ds}\right)}\right] = \frac{1}{2\mathrm{Ca}}, \tag{3.4.12}$$

when combined with the stress boundary condition, this can be expressed equivalently in the ζ-plane as

$$\mathrm{Re}\left[\frac{2F(\zeta)}{\zeta z_\zeta}\right] = \frac{1}{2\mathrm{Ca}|z_\zeta|}, \tag{3.4.13}$$

where $z_\zeta \equiv \frac{dz}{d\zeta}$. When one subtracts off terms of $1/\zeta^2$ and $1/\zeta$ from this kinematic boundary condition, Eq. (3.4.13) becomes

$$\mathrm{Re}\left[\frac{F(\zeta)}{\zeta z_\zeta} - \frac{D}{\zeta^2} - \frac{C}{\zeta}\right] = \frac{1}{4\mathrm{Ca}|z_\zeta|} - \mathrm{Re}\left[\frac{D}{\zeta^2} + \frac{C}{\zeta}\right] = \frac{1}{4\mathrm{Ca}|z_\zeta|} - \mathrm{Re}\left[\overline{D}\zeta^2 + \overline{C}\zeta\right]. \tag{3.4.14}$$

Because $F(\zeta)$ has a simple pole at $\zeta = 0$, the function in the square brackets on the left-hand side of Eq. (3.4.14) is analytic everywhere inside ζ, with the suitable choice of constants C and D. Consequently, because the real part of an analytic function is now known on the boundary of the unit circle, we may apply the Poisson Integral Formula to obtain

$$F(\zeta) = \zeta z_\zeta(\zeta)\left[\frac{I(\zeta)}{\mathrm{Ca}} + \frac{D}{\zeta^2} + \frac{C}{\zeta} - \overline{D}\zeta^2 - \overline{C}\zeta + \mathrm{i}b\right] \tag{3.4.15}$$

where b is some real constant and

$$I(\zeta) = \frac{1}{8\pi\mathrm{i}}\oint_{|\zeta'|=1} \frac{d\zeta'}{\zeta'}\frac{\zeta'+\zeta}{\zeta'-\zeta}\frac{1}{|z_\zeta(\zeta')|}. \tag{3.4.16}$$

Note that the Poisson Integral Formula gives the analytic function everywhere inside a simply connected domain, given the real part of that function on the boundary. Thus, once the map $z(\zeta)$ and the constants b, C and D are known, we have an explicit expression for $F(\zeta)$. Then, if the map is known *a priori*, one needs to consider the far-field behavior of $F(\zeta)$, in order to determine the unknown constants.

Due to a second-order pole of $z_\zeta(\zeta)$ at $\zeta = -\mathrm{i}$ (3.4.1), the quantity inside the brackets in expression (3.4.15), and its derivative must vanish at $\zeta = -\mathrm{i}$ so that it remains analytic at $\zeta = -\mathrm{i}$. Therefore, in this limit, we have

$$\frac{I(\zeta)}{\mathrm{Ca}} + \frac{D}{\zeta^2} + \frac{C}{\zeta} - \overline{D}\zeta^2 - \overline{C}\zeta + \mathrm{i}b = A(\zeta+\mathrm{i})^2 + \ldots \tag{3.4.17}$$

for some complex constant A which is related to f_∞ by

$$\mathrm{i}aA = f_\infty, \tag{3.4.18}$$

based on $F \equiv f \to f_\infty$ as $z(\zeta \to -\mathrm{i}) \to \infty$. This signifies that

$$\frac{I(-\mathrm{i})}{\mathrm{Ca}} - D + \overline{D} + \mathrm{i}C + \mathrm{i}\overline{C} + \mathrm{i}b = 0, \tag{3.4.19}$$

and, after differentiating once,

$$\frac{I_\zeta(-\mathrm{i})}{\mathrm{Ca}} + 2\mathrm{i}D + C + 2\overline{D}\mathrm{i} - \overline{C} = 0, \tag{3.4.20}$$

eliminating b from the expression. Then by differentiating the left hand side of Eq. (3.4.17) twice and evaluating it at $\zeta = -\mathrm{i}$, we obtain

$$A = \frac{1}{2}\left[\frac{I_{\zeta\zeta}(-\mathrm{i})}{\mathrm{Ca}} + 6D - 2C\mathrm{i} - 2\overline{D}\right], \tag{3.4.21}$$

which, combined with Eq. (3.4.18), leads to

$$-\frac{1}{2} = \mathrm{Re}\left[\frac{\mathrm{i}a}{2}\left[\frac{I_{\zeta\zeta}(-\mathrm{i})}{\mathrm{Ca}} + 6D - 2C\mathrm{i} - 2\overline{D}\right]\right]. \tag{3.4.22}$$

These equations, along with the steady state condition, come together to yield values for C and D. The case for $n = 1$ will be explicitly worked out in §3.4.2.

When the expression for $F(\zeta)$ is found, we can now solve for $G(\zeta)$ by Eq. (3.4.5), or

$$G(\zeta) = -\overline{z}(\zeta^{-1})F(\zeta). \tag{3.4.23}$$

This condition shows there exists some constraint on the singularities of $G(\zeta)$ imposed by the singularities of the conformal mapping function $z(\zeta)$ and by $F(\zeta)$. If we allow $z(\zeta)$ to be written as

$$z(\zeta) = \frac{a}{\zeta + \mathrm{i}} + a_0 + \sum_{k=1}^{n} a_k\zeta^k \tag{3.4.24}$$

where $n \geq 1$ is some positive integer, then

$$\overline{z}(\zeta^{-1}) = \frac{\overline{a}\zeta}{1 - \mathrm{i}\zeta} + \overline{a_0} + \sum_{k=1}^{n} \frac{\overline{a_k}}{\zeta^k}. \tag{3.4.25}$$

Since $F(\zeta) = \mathcal{O}(\zeta^{-1})$ as $\zeta \to 0$, combining equations (3.4.43) and (3.4.25) indicates that, near $\zeta = 0$, $G(\zeta)$ behaves as

$$G(\zeta) = \frac{G_{-(n+1)}}{\zeta^{n+1}} + \frac{G_{-n}}{\zeta^{n}} + \cdots + \frac{G_{-1}}{\zeta} + G_0 + G_1\zeta + \ldots, \tag{3.4.26}$$

corresponding to

$$g(z) = \frac{g_{-(n+1)}}{(z - z_d)^{n+1}} + \text{higher order terms} \tag{3.4.27}$$

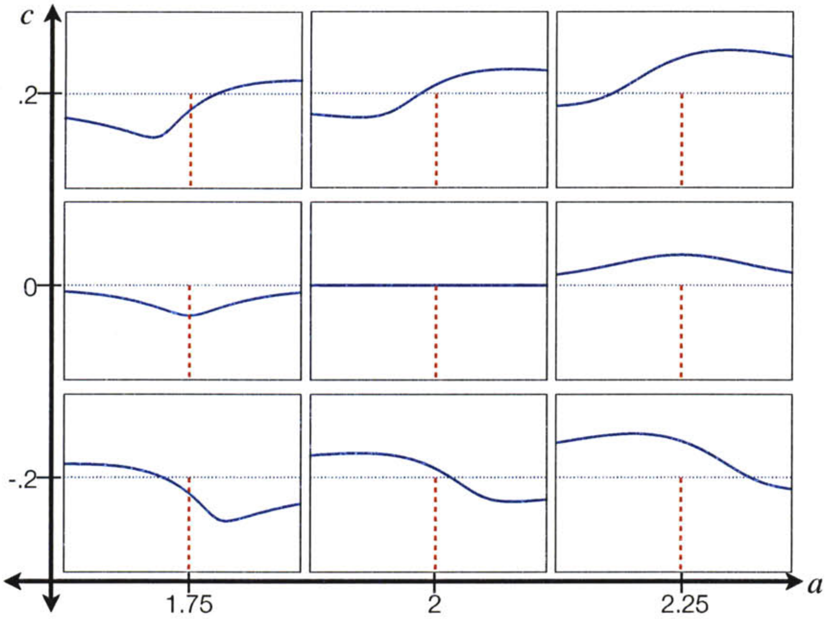

Figure 3.4.2: The geometrical significance of parameters a and c for $n = 1$. The flat interface corresponds to $a = 2, c = 0$. Increasing (decreasing) a above 2 with $c = 0$ (along the horizontal axis) moves the interface up (down) in a left-right symmetric fashion. Non-zero values of c (along the vertical axis) introduce left-right asymmetry.

near z_d in the physical domain, which has physical implications. For instance, for $n = 1$, $g(z)$ has a potential dipole and a quadrupole. Interpreting n as a measure of the perturbations in the free surface away from a flat state, we see that $g(z)$ will have increasingly higher-order singularities with increasing n. In physical terms, the swimmer is required to generate more complex swimming patterns (corresponding to multipoles of $g(z)$) in order to swim beneath free surfaces of various and possibly more complicated deformations.

3.4.2 Complete solution: n=1

In the simplest non-trivial case of $n = 1$, the conformal map reduces to

$$z(\zeta) = \frac{a}{\zeta + \mathrm{i}} + a_0 + a_1\zeta, \tag{3.4.28}$$

where a, a_0 and a_1 are complex numbers. The map has three degrees of freedom, two of which pertain to the swimmer's position corresponding to the origin of the unit circle (i.e. $z(\zeta = 0) \equiv z_d = -\mathrm{i}$). This complex condition leads to

$$a_0 = (a - 1)\mathrm{i}. \tag{3.4.29}$$

The third degree of freedom matches the position $\zeta = -\mathrm{i}$ to the point at which the free surface extends to infinity in the physical domain. Accordingly, one can see that $z(\zeta)$ becomes singular as $\zeta \to -\mathrm{i}$. Furthermore, in this limit, the interface is expected to be flat, meaning the imaginary part of $z(\zeta \to -\mathrm{i})$ should vanish. This is equivalent to $z(\zeta) - \overline{z}(1/\zeta) = 0$, where $\overline{z}(1/\zeta)$ can be written as

$$\overline{z}(1/\zeta) = \frac{a}{\zeta + \mathrm{i}} + \overline{a}_0 + \mathrm{i}a + \frac{\overline{a}_1}{\zeta}. \tag{3.4.30}$$

Then by combining this far-field condition with $a_0 = (a - 1)\mathrm{i}$ yields

$$\mathrm{Re}[a_1] = \frac{a}{2} - 1, \tag{3.4.31}$$

and now the map can be determined completely by two real parameters, a and c:

$$z(\zeta) = \frac{a}{\zeta + \mathrm{i}} + \mathrm{i}(a - 1) + \left(\frac{a}{2} - 1 + \mathrm{i}c\right)\zeta. \tag{3.4.32}$$

where a and c describe the size and asymmetry of the free surface deformations, respectively. When $a = 2$ with $c = 0$ the interface is flat; increasing a above 2 corresponds to a symmetric *upward* deformation of the interface; decreasing a below 2 leads to a symmetric *downward* deformation. Changing the value of c away from zero introduces left-right *asymmetry* of the free surface deformation about a vertical axis through the swimmer, as illustrated in Figure 3.4.2.

Letting $n = 1$ places a constraint on the types of singularities that model the swimmer. Specifically, we know that the swimmer is a stresslet with a superposed potential quadrupole and dipole, meaning

$$g(z) = \frac{q^*}{(z+\mathrm{i})^2} + \frac{(-\mathrm{i}s^* + d^*)}{(z+\mathrm{i})} + g_0 + g_1(z+\mathrm{i}) + ..., \tag{3.4.33}$$

near the swimmer position $z_d \equiv -\mathrm{i}$. Here, s^* and q^* correspond to the stresset and quadrupole strengths, respectively, while d^* is the dipole strength after the contribution $-s^*\overline{z_d} = -\mathrm{i}s^*$ associated with the stresslet at $z_d = -\mathrm{i}$ has been subtracted off (see Eq. (3.3.2)).

Because we are in a co-moving frame, the velocity of the swimmer should vanish, which is equivalent to the finite part of $u + \mathrm{i}v$ at $z = z_d$ being zero. Since, for $n = 1$,

$$f(z) = \frac{s^*}{z+\mathrm{i}} + f_0 + f_1(z+\mathrm{i}) + \ldots, \quad g(z) = \frac{q^*}{(z+\mathrm{i})^2} + \frac{(-\mathrm{i}s^* + d^*)}{(z+\mathrm{i})} + g_0 + g_1(z+\mathrm{i}) + \ldots, \tag{3.4.34}$$

the finite part of the velocity at $z = z_d$ is given by

$$-f_0 + z_d\overline{f_1} + \overline{g_1} = 0. \tag{3.4.35}$$

Based on the Residue Theorem, the terms f_0, f_1 and g_1 are written as

$$f_0 = \frac{1}{2\pi\mathrm{i}} \oint_\Gamma \frac{F(\zeta)}{(z(\zeta) - z_d)} \frac{dz}{d\zeta}\, d\zeta, \quad f_1 = \frac{1}{2\pi\mathrm{i}} \oint_\Gamma \frac{F(\zeta)}{(z(\zeta) - z_d)^2} \frac{dz}{d\zeta}\, d\zeta,$$
$$g_1 = -\frac{1}{2\pi\mathrm{i}} \oint_\Gamma \frac{\overline{z}(1/\zeta)F(\zeta)}{(z(\zeta) - z_d)^2} \frac{dz}{d\zeta}\, d\zeta \tag{3.4.36}$$

where Γ is any simple closed curve surrounding $\zeta = 0$.

As previously mentioned, we first fix the free surface shape (i.e. the values of a, c known) and state state velocity U. The values of the constants C and D can then be found by simultaneously solving

$$-f_0 + z_d\overline{f_1} + \overline{g_1} = 0, \tag{3.4.37}$$

which is a complex equation, together with the real equation (3.4.20), i.e.,

$$\frac{I_\zeta(-\mathrm{i})}{\mathrm{Ca}} + 2\mathrm{i}D + C + 2\overline{D}\mathrm{i} - \overline{C} = 0, \tag{3.4.38}$$

and finally the real equation

$$-\frac{1}{2} = \mathrm{Re}\left[\frac{\mathrm{i}a}{2}\left[\frac{I_{\zeta\zeta}(-\mathrm{i})}{\mathrm{Ca}} + 6D - 2C\mathrm{i} - 2\overline{D}\right]\right]. \tag{3.4.39}$$

Once C and D are found accordingly, the Goursat functions $F(\zeta)$ and $G(\zeta)$ can be fully determined in the closed form. This means that *everything* about the flow field is now known, since all the physical variables, such as pressure and velocity field, can be expressed in terms of $f(z) \equiv F(\zeta)$ and $g(z) \equiv G(\zeta)$. The associated singularity strengths — stresslet, dipole and quadrupole, can be readily computed also; here they are calculated for $a = 2, c = 0$ (the flat interface case):

$$s^* = 2\mathrm{i}, \quad d^* = -4, \quad q^* = 0, \tag{3.4.40}$$

which correspond precisely to the results derived using the method of images for the same interface, as shown in Appendix A.2. Keep in mind that the method of images is only valid for flat interfaces, and our analysis has generalized it for arbitrary shapes of the free surface.

Summary of results: $n = 1$

In this section, we list the key formulae and results for $n = 1$ for clarity and completeness. The conformal mapping that transforms the unit ζ-disc to the physical domain is given by

$$z(\zeta) = \frac{a}{\zeta + \mathrm{i}} + \mathrm{i}(a-1) + \left(\frac{a}{2} - 1 + \mathrm{i}c\right)\zeta, \tag{3.4.41}$$

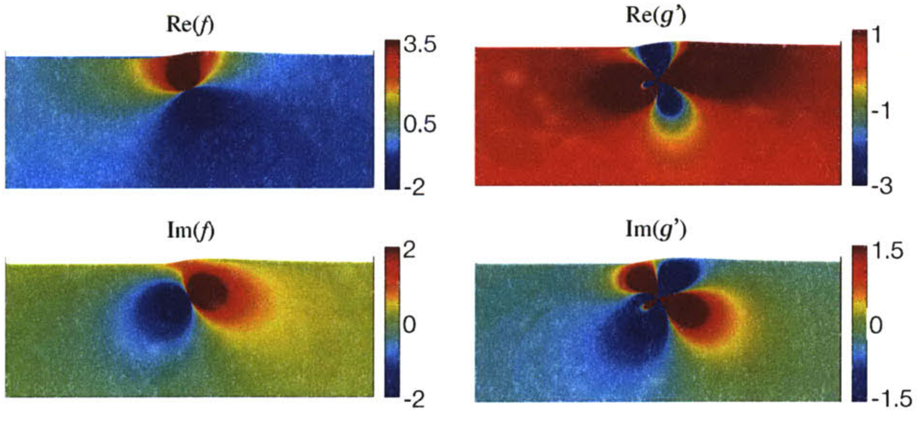

(a) (b)

Figure 3.4.3: For an interface shape $a = 2.1$ and $c = 0.1$ ($n = 1$), the corresponding functions $f(z)$ and $g'(z)$ are shown in (a) and (b), respectively.

where a and c are real parameters. The corresponding Goursat functions determining the associated steady-state velocity field are

$$F(\zeta) = \zeta z_\zeta(\zeta)\left[\frac{I(\zeta)}{\mathrm{Ca}} + \frac{D}{\zeta^2} + \frac{C}{\zeta} - \overline{D}\zeta^2 - \overline{C}\zeta + \mathrm{i}b\right] \tag{3.4.42}$$

and

$$G(\zeta) = -\overline{z}(\zeta^{-1})F(\zeta). \tag{3.4.43}$$

The integral $I(\zeta)$ is given by

$$I(\zeta) = \frac{1}{8\pi\mathrm{i}}\oint_{|\zeta'|=1}\frac{d\zeta'}{\zeta'}\frac{\zeta'+\zeta}{\zeta'-\zeta}\frac{1}{|z_\zeta(\zeta')|}, \tag{3.4.44}$$

the constant b is given (from Eq. (3.4.19)) by

$$b = \frac{\mathrm{i}I(-\mathrm{i})}{\mathrm{Ca}} - \mathrm{i}D + \mathrm{i}\overline{D} - C - \overline{C}, \tag{3.4.45}$$

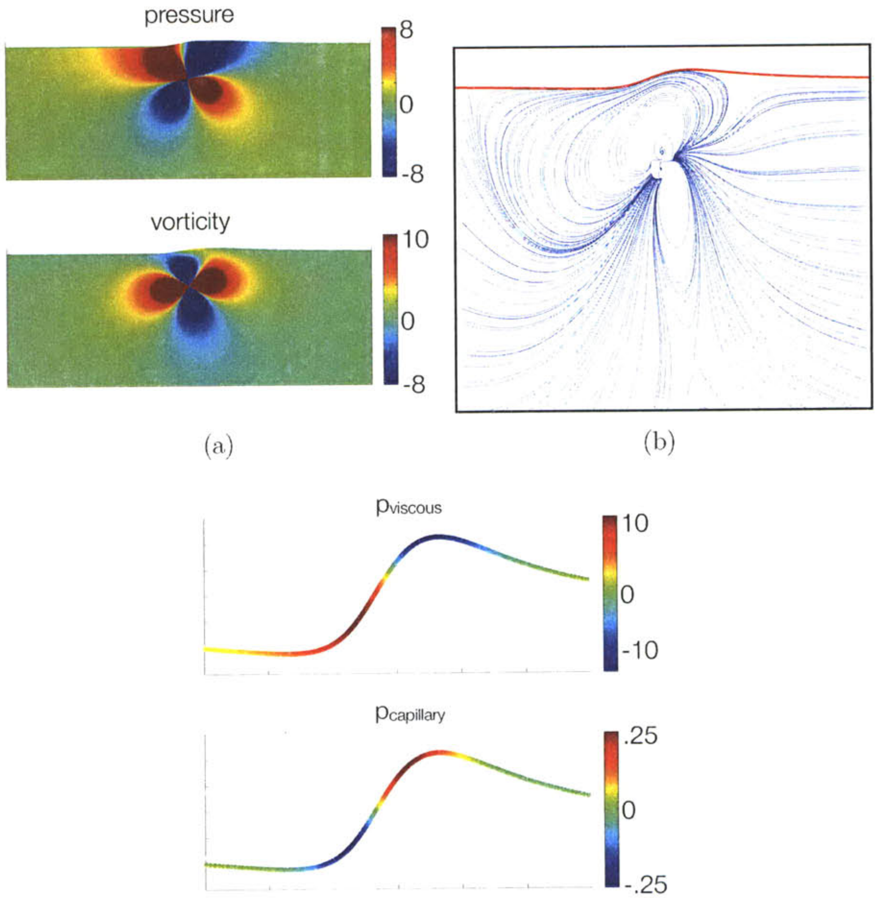

(a) (b)

(c)

Figure 3.4.4: For an interface shape $a = 2.1$ and $c = 0.1$ ($n = 1$), the resulting streamlines are plotted in (b). The flow inside the domain is described completely by two complex functions, f and g, obtained analytically using the conformal mapping technique. The resultant pressure field as well as the vorticity field is shown in (a). Note that low pressure underneath the "bump" is generated by viscous stresses that dominate over capillary effects, as illustrated in (c).

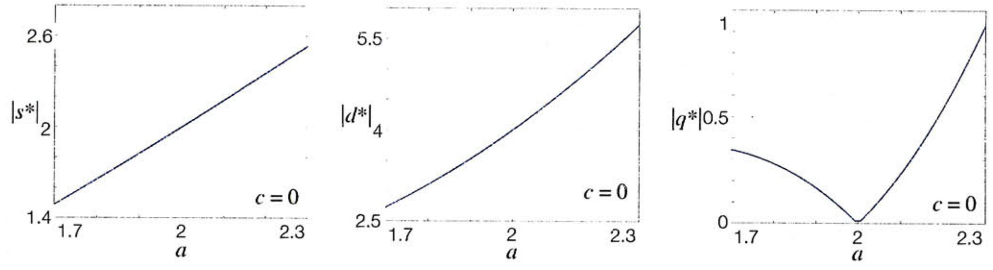

(a) (b) (c)

Figure 3.4.5: The singularity strengths, (a) stresslet $|s^*|$ (b) dipole $|d^*|$ and and (c) quadrupole $|q^*|$ as the interface transitions from a downward deformation ($a < 2$) to an upward deformation ($a > 2$) with $c = 0$. Note that the quadrupole is absent ($q^* = 0$) when $a = 2$ (the flat interface case) but its strength increases for $a \neq 2$ (the deformed interface case).

and C and D are two complex constants determined from the linear system of (four real) equations:

$$\begin{aligned} 0 &= \frac{I_\zeta(-\mathrm{i})}{\mathrm{Ca}} + 2\mathrm{i}D + C + 2\overline{D}\mathrm{i} - \overline{C}, \quad \text{(real equation)} \\ -\frac{1}{2} &= \mathrm{Re}\left[\frac{\mathrm{i}a}{2}\left[\frac{I_{\zeta\zeta}(-\mathrm{i})}{\mathrm{Ca}} + 6D - 2C\mathrm{i} - 2\overline{D}\right]\right], \quad \text{(real equation)} \\ 0 &= -f_0 - \mathrm{i}\overline{f_1} + \overline{g_1} \quad \text{(complex equation)}, \end{aligned} \tag{3.4.46}$$

where f_0, f_1 and g_1 depend linearly on C and D. Putting them in a physical context, the first equation in (3.4.46) stems from the analyticity of $F(\zeta)$ in the far-field, while the second equation is enforced by the finite velocity condition (in the co-translating frame) at infinity. The last complex equation is derived from the steady state motion of the swimmer. Solutions for a specific interfacial shape (i.e. $a = 2.1$, $c = 0.1$) are plotted in Figures 3.4.3 and 3.4.4.

One fact becomes immediately clear from the new solutions. From the method of images analysis in Appendix A.2, it is known that a point stresslet with a superposed potential dipole can translate steadily beneath an undeformed (i.e. flat) free surface. However, as soon as the interface becomes deformed, it is necessary for the stresslet and potential dipole to be supplemented with a higher order potential singularity. In the case of the $n = 1$ solutions this singularity is a quadrupole. Figure 3.4.5 shows graphs of the magnitude of the stresslet, dipole and quadrupole strengths for the $n = 1$ case as functions of a (with $c = 0$, so the free surface profiles are all left-right symmetric). Note that the quadrupole strength vanishes when $a = 2$ (the flat state) but necessarily becomes non-zero when the interface deforms ($a \neq 2$).

The approach we have taken here differs from many swimming formulations in which the deformation of the swimmer is prescribed and the resulting swimming velocity (and interfacial deformation) is computed. Instead, we find that it is more convenient to specify the swimming velocity and interface shape and determine the corresponding squirming protocol. We assume the steady state velocity of the swimmer as well as the shape of the interface (fixed by two parameters, a and c for $n = 1$) as known and solve for the singularities (s^*, d^*, and q^* for $n = 1$) that satisfy the given steady state condition. This is the inverse of a typical swimming problem in which one assumes that the swimmer only has a direct control over its own deformations ("squirming"), which leads to the deformation of the free surface as determined by the fluid properties as well as the local flow created by the swimmer (see Figure 3.4.2). This "forward" approach (given a swimmer, find the swimming velocity) is practical in the analysis of a particular swimming organism or device. However, for questions related to design, synthesis, and optimizations, frequently the inverse approach is more useful as one can specify a desired output and compute the corresponding required forcing (i.e. singularity strengths). Our formulation is particularly well-adapted for the *inverse* approach since the analysis becomes linear as seen in Eq. (3.4.46).

Mechanism of symmetry-breaking

It is easy to lose sight of the physics amongst all the details of the analysis. In order to re-orient ourselves, we spend a minute here to elaborate on the physical mechanism of swimming. As stated in the introduction, the model swimmer is able to generate only completely symmetric "squirming" motions so that it is unable to swim in an unbounded fluid. In other words, any kind of geometrical variation in the environment (such as the presence of *any* surface) will create the necessary asymmetry

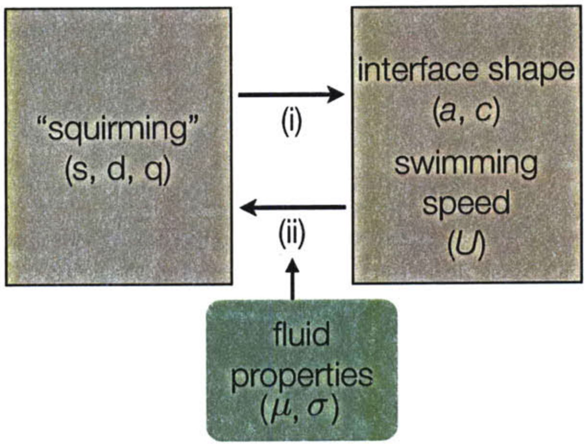
"squirming"
(s, d, q)
(i)
interface shape
(a, c)
swimming
speed
(U)
(ii)
fluid
properties
(μ, σ)

Figure 3.4.6: The swimmer creates a local flow by "squirming", represented mathematically by singularities (i.e. for $n = 1$, a stresslet, dipole, and quadrupole). Depending on the fluid properties such as surface tension σ and viscosity μ, this local flow interacts with the free surface, and this interplay advects the swimmer. Thus, the arrow (i) represents a "forward" (analysis) approach to the problem. However, we solve the *inverse* (synthesis) problem (represented by arrow (ii)).

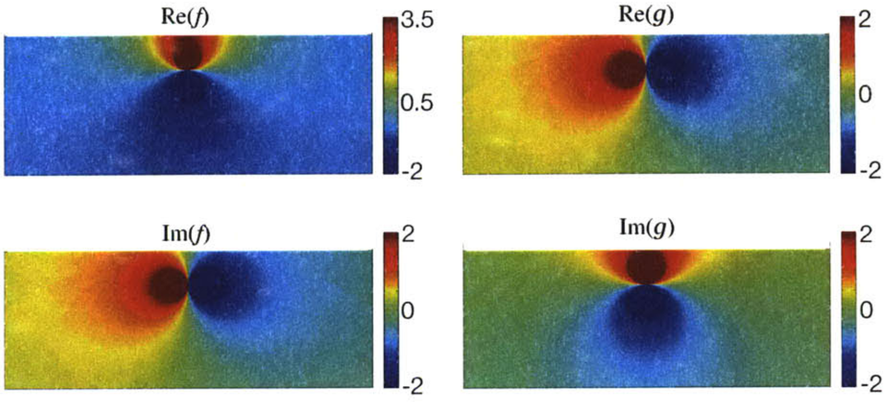

(a)

(b)

Figure 3.4.7: The solutions $f(z)$ and $g(z)$ for a flat interface $a = 2$ and $c = 0$ ($n = 1$) are shown in (a) and (b), respectively. These plots can be thought of the effective behaviors of the singularities of $f(z)$ and $g(z)$, in this case, a stresslet and a potential dipole

in the system essential for propulsion. It is important to recognize that the present surface (for example) does not need to contain asymmetry. This means that the surface does not even need to be deformable in our framework to enable motion, and in particular, does not need to be deformed (either symmetrically or asymmetrically) for the swimmer to generate motion. In order to understand this subtle point, we examine the Goursat solutions plotted in Figure 3.4.7, that correspond to the completely flat interface case.

If one considers the real and imaginary parts of $f(z)$ and $g(z)$ separately, there appears to be nothing in the system to break the left-right symmetry *directly*. However, when the parts of $f(z)$ and $g(z)$ are superimposed, one can see that, overall, the singularities must act at roughly 45 degrees off the vertical. If the interface were not present, the system would still be completely symmetric. However, the interface interacts with the singularities acting *at an angle*, which breaks the left-right symmetry. In essence, the swimmer pulls and pushes on the fluid at an angle towards the interface. If such swimmer acted either completely perpendicular to or parallel to the (flat or symmetric) interface, it would not be able to break the left-right symmetry to move forward. But by doing so off the axes, the swimmer is able to take advantage of the free surface and propel itself.

To summarize, we have developed a robust framework for analyzing swimming near free surfaces. The swimmer squirms in some fashion (modeled as a sum of mathematical singularities) and creates a local flow that affects the shape of the interface. Because this interaction between the swimmer's squirming, the free surface, and the subsequent motion of the swimmer is highly nonlinear, the derivation of closed-form solutions to describe this phenomenon is a non-trivial task. By employing conformal mapping techniques, we obtain these solutions in the steady-state limit, without putting any geometrical constraints on the free surface. The usefulness of these exact solutions is highlighted in Chapter 4, as we apply them to answer more physically relevant questions that pertain to optimization.

Chapter 4

Optimal swimming near free surfaces

4.1 Optimization in low Reynolds locomotion

Low Reynolds locomotion is an active area of study, especially in light of the growing interest in the mechanics of microorganisms and small-scale robotics in biological applications. Such studies include questions related to optimization, which often focus on a particular type of swimmer. One example is the three-link swimmer, introduced by E. M. Purcell [56] as the simplest imaginary swimmer that can break symmetry in the Stokes regime. Made of three slender rods connected by two hinges, this swimmer propels itself by moving its front and rear segments alternatively, as shown in Figure 4.1.1. Because of its simplicity, the three-link swimmer was an ideal subject for optimization studies. Becker *et al.* [7] calculated the optimal stroke angles that minimize the total mechanical work required to generate motion. The optimal angles were shown to depend on the length of the two outer rods relative to that of the inner rod. In contrast to this study which optimized the geometry of the swimmer, Tam and Hosoi [67] considered a device with a *fixed* geometry and sought the most optimal stroke patterns that maximize the swimming efficiency and speed, respectively.

Low Re swimming can be modeled by representing the swimming stroke as a series

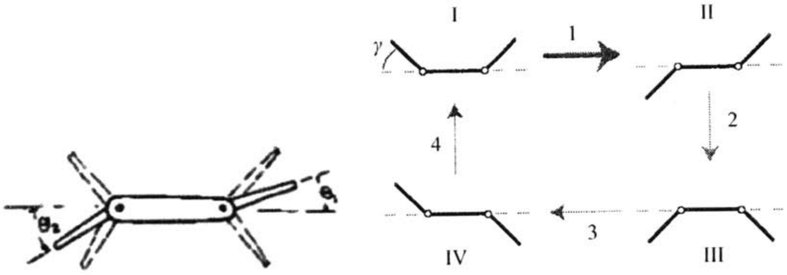

(a) (b)

Figure 4.1.1: (a) Purcell's three-link swimmer, as introduced in his lecture, consists of three rods and can generate non-reciprocal motion by moving the rods alternatively (image reproduced from [56]. One example of a swimming sequence is shown in (b) [7].

of changing geometries. Focusing on this idea, Shapere and Wilczek [61] found that swimmer geometries associated with the maximum efficiency are symmetric about the axis of propulsion. This work was generalized by Avron *et al.* [5] who used conformal mapping techniques to include large deformations of the body. They showed that the swimming efficiency tends to *decrease* both for small and large deformations of the body, while intermediate deformations are optimal.

In all of these cases, the question of optimization is limited to an isolated low Reynolds swimmer moving in an *unbounded* fluid. While these studies have been instrumental in understanding the fundamental mechanism of self-propulsion in the Stokes regime, one may wish to consider variations in the swimming environment, such as the presence of external surfaces. In general, the presence of a deformable surface, such as an air-water interface, complicates the analysis due to the nonlinear coupling between the evolving shape of the interface and the swimmer's motion. Now thanks to the closed-form solutions derived in Chapter 3, we can extend the question of optimization to *include* the effects of free surfaces. This is particularly interesting in light of the known effect of "free surface swimming" in moderate to high Reynolds number flows. Due to the energetic cost associated with creating surface waves, swimmers in this Reynolds regime tend to swim less efficiently as they approach the free surface [32]. However, for a low Reynolds swimmer that *utilizes* the free surface, we prove in this chapter that its proximity to the free surface is energetically favorable.

Furthermore, we solve for the optimal free surface shapes that correspond to the most efficient modes of swimming.

4.2 Mathematical setup

What is *optimal*?

Every optimization procedure contains at least one parameter that one hopes to either minimize or to maximize, depending on the context. It is very common to *maximize efficiency*, where efficiency is most generally defined as the ratio of *useful work* to *total work*. More specific to locomotion, efficiency is usually the power required to pull the swimmer at some translational speed (i.e. the product of the drag force on the swimmer and its velocity) divided by the total power dissipated. However, because our solution guarantees that the swimmer translates at a unit speed, the numerator is a fixed value. Hence, we seek to *minimize* the denominator, or the rate of total viscous dissipation in the fluid domain.

4.2.1 Calculating and minimizing the rate of viscous dissipation

There exists an inherent difficulty in calculating the total dissipative power, due to the presence of singularities in our system. A singularity causes the dissipation to diverge, overwhelming any dissipative differences in our integrated flow fields generated by different combinations of singularities. In order to circumvent this problem, we regularize the rate of total dissipation by taking a finite sized hole of dimensionless radius $R \equiv \frac{\hat{R}}{\hat{h}}$ around the swimmer, as shown in Appendix B. While this approach may not be the most sophisticated way to regularize our solution, R introduces a new length scale into our system which can be interpreted as restoring a finite-size to the swimmer relative to its distance from the interface. Strictly speaking, in order for the singularity description of the swimmer to be valid, the circle around the swimmer needs to be well separated from the interface, meaning $R < 1$.

For a given free surface shape, one can find $f(z)$ and $g(z)$ (see Chapter 3). These solutions lead to an expression for the rate of viscous dissipation E in the domain ∂D bounded by a free surface and a hole of size R:

$$E = \frac{1}{2i} \oint\limits_{\partial D} \left[z\overline{z} f'' \overline{f'} - z f'' \overline{f} + z g'' \overline{f'} + g'' \overline{g'} \right] dz - \frac{1}{2i} \oint\limits_{\partial D} \overline{z g''} f' d\overline{z}, \tag{4.2.1}$$

and the detailed calculation is shown in Appendix B. By comparing the values of dissipation for different free surface shapes (i.e. varying shape parameters, a and c), we find the rate of *minimum* viscous dissipation E_{min} along with the corresponding shapes of the free surface, a_{opt} and c_{opt}. In the previous works mentioned in §4.1, the goal is often to find the detailed swimming strokes that yield the most energetically favorable motion. With a swimmer's stroke represented as a sum of singularities in our formulation, we can equivalently ask which linear combination of singularities, or which free surface shape (a_{opt} and c_{opt}) results in the least amount of viscous dissipation. Recall that there is a one-to-one correspondence between a unique set of singularities which describe the swimming stroke and a steady state solution of the free surface shape. This approach not only addresses the relationship between the swimmer's stroke and the overall power dissipation, but it also highlights the role of the free surface in our problem. In summary, one can now pose the following two questions: "Is it energetically favorable for a swimmer translating beneath a free surface to deform the surface? And if so, what is the resultant optimal free surface shape?" The answers to these questions will be discussed in §4.3.2. A more fundamental question pertains to the swimmer's proximity to the free surface, namely "Is it energetically favorable for the swimmer to be close to the surface?" which will be answered in the following section.

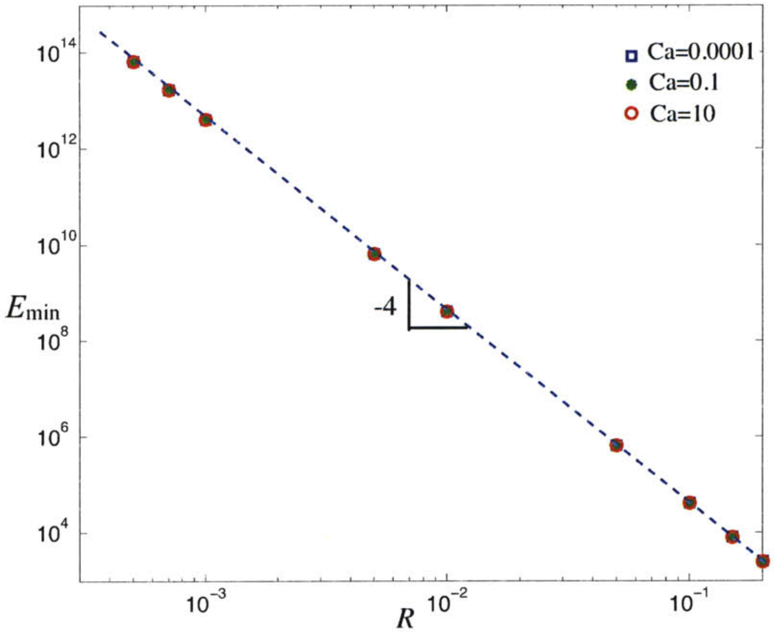

Figure 4.3.1: The rate of minimum dissipation, E_{min}, in the system is shown to vary as R^{-4} (where R is the "cutoff" radius), independent of the the capillary number, Ca.

4.3 Results

4.3.1 Proximity to the interface

Figure 4.3.1 shows the power law relationship between the rate of minimum dissipation, $E_{\min}$ and the cutoff radius, R, which holds true independent of capillary number, Ca. Recalling that $E_{\min}$ has been scaled by $\mu\widehat{U}^2$, this minimum dissipative rate can be expressed in dimensional terms as:

$$\widehat{E}_{\min} \sim \frac{\mu\widehat{U}^2\widehat{h}^4}{\widehat{R}^4}, \tag{4.3.1}$$

indicating that with increasing viscosity, μ, and increasing swimming speed, $\widehat{U}$, the rate of total *minimum* viscous dissipation increases. The strong dependence of $\widehat{E}_{\min}$ on the distance to the interface is particularly revealing. The minimum dissipative rate is shown to decrease (to the fourth power), the closer the swimmer is to the free surface, relative to its size. Thus, for a low Reynolds swimmer that relies on the presence of the free surface to swim, it is energetically favorable for the swimmer to be *closer* to the surface.

This result can be compared to a low Reynolds swimmer moving at speed $\widehat{U}$ in an *unbounded* fluid. The viscous dissipation for this swimmer scales as $\mu\widehat{U}^2$, implying that for $\left(\frac{\widehat{h}}{\widehat{R}}\right)^4 < 1$, the swimmer near the free surface dissipates less energy than its counterpart in an unbounded domain. Keep in mind that this result needs to be considered with caution since our solution requires that $R \equiv \frac{\widehat{R}}{\widehat{h}} < 1$. Finally, it is noteworthy that surface tension, σ, does not appear in this expression of dimensional minimum dissipation. However, as we will see, surface tension plays an important role in the swimmer's selection of optimal free surface shapes.

4.3.2 Optimal free surface shapes

As shown in Figure 4.3.2, the optimal free surface shapes depend on both the fluid properties — in the form of capillary number Ca — and R, the cutoff radius. At low values of Ca, the interface is difficult to deform (high surface tension). Not surprisingly, in this limit, the optimal interface shape is shown to be flat ($\Delta a_{\text{opt}} = 0$, where $\Delta a_{\text{opt}} \equiv 2 - a_{\text{opt}}$, and $c_{\text{opt}} = 0$), regardless of the value of R. As Ca increases above some critical value (Ca_{crit1}), the free surface forms a small symmetric "dip" toward the swimmer ($\Delta a_{\text{opt}} > 0$ and $c_{\text{opt}} = 0$). Finally when Ca reaches another critical limit (Ca_{crit2}), the deformation saturates at some maximum value. These two distinct sets of critical capillary numbers are shown in Figure 4.3.3 and exhibit a linear dependence on R. While the magnitude of Δa_{opt} varies with R (Figure 4.3.2 and 4.3.4), it consistently shares the same general trend in Ca for all values of R, the implications of which will be investigated shortly.

The fact that the optimal free surface shapes are completely symmetric (i.e. $c_{\text{opt}} = 0$) provides a way to simplify the exact solutions. Because the existing exact solutions for general asymmetric deformations are extremely long and complicated, the only practical way to extract physical intuition from them (such as power laws) is by plotting them. Fortunately, when $c \equiv 0$, these equations reduce considerably,

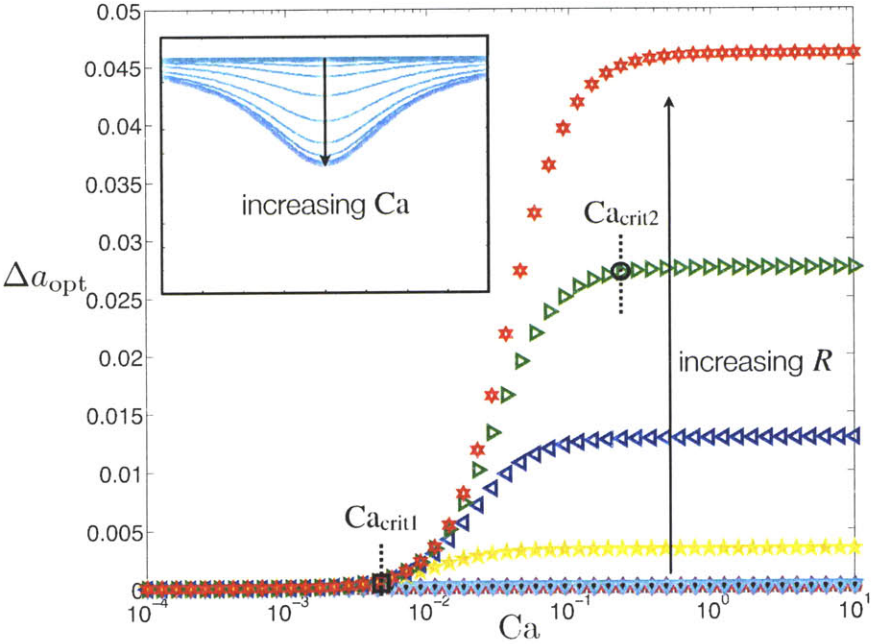

Figure 4.3.2: The value of $\Delta a_{\mathrm{opt}} \equiv 2 - a_{\mathrm{opt}}$, the measure of deviation from the flat interface, as a function of the capillary number, Ca for different values of R. As expected, in the limit of low Ca (high surface tension) as well as $R \to 0$, the interface remains flat (i.e. $\Delta a_{\mathrm{opt}} = 0$, $c = 0$). As Ca increases (low surface tension), a small dip ($\Delta a_{\mathrm{opt}} > 0$) begins to grow. As Ca continues to increase, this deflection saturates at some maximum Δa_{opt} value that varies with R. The free surface shapes that correspond to the most energy efficient steady state solutions as a function of capillary number, Ca are shown in the inset. In all cases, c_{opt}, the measure of asymmetry, remains approximately zero.

allowing one to derive asymptotic solutions in the limit of small deformations. The full equations for both general asymmetric deformations and symmetric ones are included in Appendix C.1. The insight provided by the asymptotic solutions will be highlighted in the following sections.

Bump up versus down

A concise answer to the question —"is it better for a swimmer to deform the free surface or not?"— depends on the capillary number and the swimmer's relative distance to the interface. However, when deformation does occur, the optimal free surface shapes are always pulled symmetrically towards the swimmer. This result can be predicted readily by perturbing the exact solutions in the limit of small symmetric

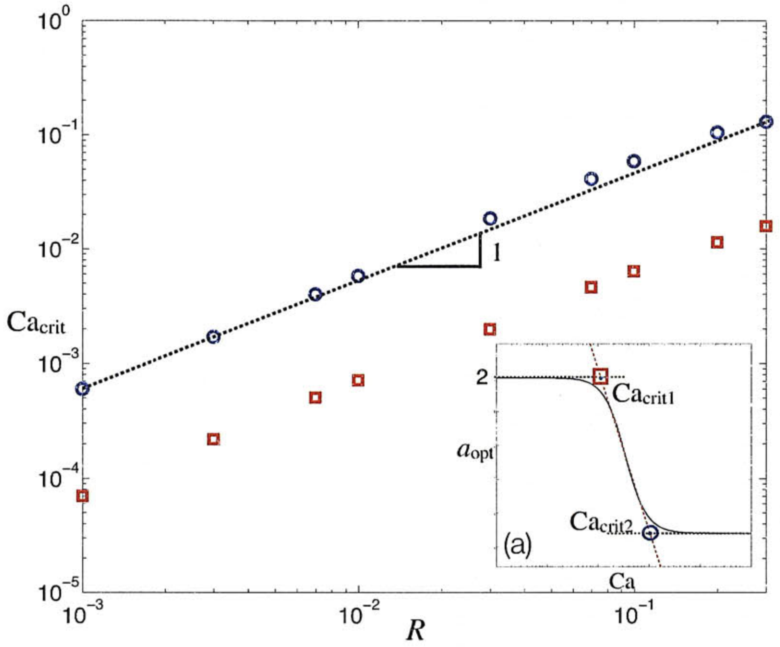

Figure 4.3.3: The value of Δa_{opt} shares the common trend of starting off at 0 and decreasing until it saturates at some maximum value. The two distinct transitions (from flat to deformed, and from deformed to maximum deformation) are marked by two sets of critical capillary numbers, as plotted here for varying values of the cutoff radius R. These critical values, $\mathrm{Ca}_{\mathrm{crit},1}$ and $\mathrm{Ca}_{\mathrm{crit},2}$, both increase linearly with R.

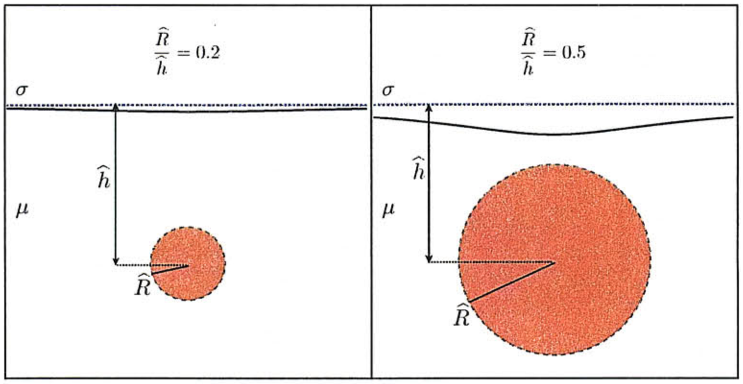
$\frac{\widehat{R}}{\widehat{h}} = 0.2$
σ
$\widehat{h}$
μ
$\widehat{R}$
$\frac{\widehat{R}}{\widehat{h}} = 0.5$
σ
$\widehat{h}$
μ
$\widehat{R}$

Figure 4.3.4: The dependance of the deformation size on the characteristic swimmer size is demonstrated for two different relative values of R.

deformations, $a \equiv 2 + \varepsilon + O(\varepsilon^2)$, where $\varepsilon \ll 1$. A positive value of ε implies the surface deformation is away from the swimmer (bump up), while a negative value corresponds to deformation towards the swimmer (bump down). By comparing the total viscous dissipation E for positive and negative ε, we see that deformation towards the swimmer ($\varepsilon < 0$) is more energetically favorable (see Figure 4.3.5). Note this solution only considers terms to the first order of ε: $E = 8\left(\frac{4}{R^4} + \frac{2}{R^2}\right) + \varepsilon h(R)$, where $h(R)$ is a positive function. (The asymptotic solutions to the second order include the dependency on Ca and are shown in Appendix C.1.1.)

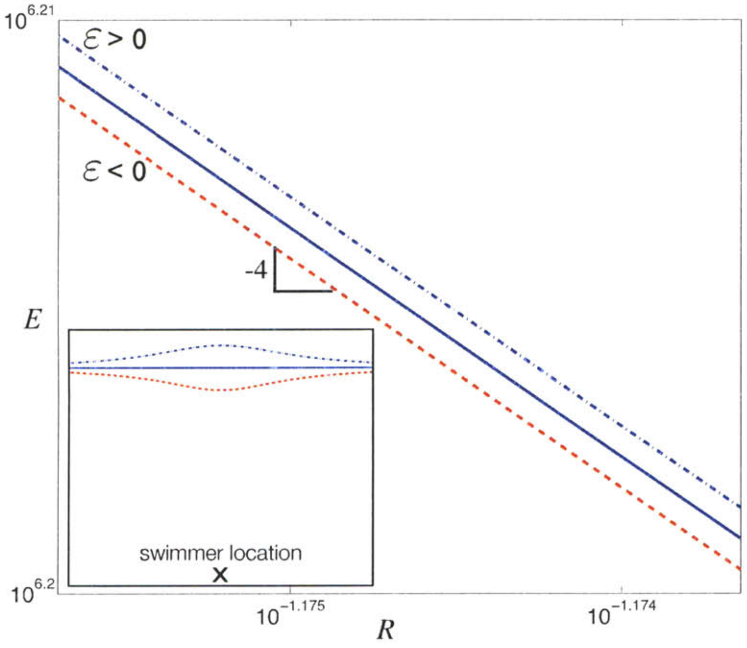

Figure 4.3.5: The rates of viscous dissipation for an asymptotically small bump up (dashed) and down (dotted) are plotted against the cutoff radius R, confirming that the bump down is more energetically favorable. Since this plot includes only the first order effects of the small perturbation solutions, it highlights the usefulness of the asymptotic analysis in predicting the physical results.

It is not immediately obvious why a bump down is more favorable than up for free surface locomotion. However, the physical reasoning may be found by borrowing ideas from the method of images approach. The method of images — valid only for flat interfaces in the strict mathematical sense — states that the free surface problem can be transformed into an unbounded one with two swimmers: one actual singularity and its "image" singularity located across the interface. The two swimmers then interact in such a way that the free surface boundary condition is satisfied at the center line between them. As shown in Figure 4.3.6, the bump down interface lowers the position of the image singularity. Since the motion of the swimmer is generated by the interaction of the image and swimmer singularities, a shorter distance between them implies that lower singularity strengths are needed to yield the same swimming velocity, reducing the viscous dissipation. However, there also exists an energetic cost associated with deforming the interface, which increases the total dissipation in the system. Due to these competing factors, the optimal surface deflection Δa_{opt} plateaus at high Ca (or low σ).

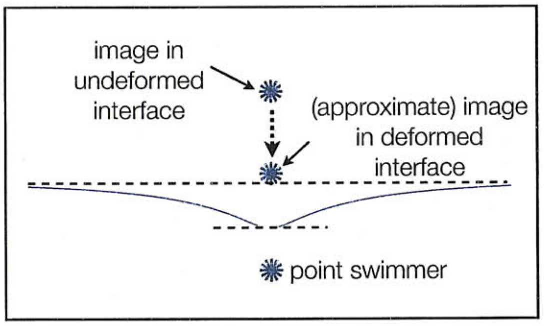
image in undeformed interface
(approximate) image in deformed interface
point swimmer

Figure 4.3.6: Deforming the interface downwards can be interpreted as bringing the image singularity closer to the swimmer. The flow is generated by the interaction between the swimmer and its image, which consequently induces the horizontal motion of the swimmer. Thus, with the image singularity closer to the swimmer, smaller singularity strengths yield the same horizontal speed (leading to reduced dissipation). However, there is also an energetic cost of deforming the interface downwards. This competition explains why the optimal downward deformation does not grow indefinitely but saturates at a critical capillary number.

Three regimes of optimal deformations

We have shown that the optimal surface shapes (expressed in terms of a size parameter, Δa_{opt}) depend on both the capillary number Ca and the cutoff radius R. When Δa_{opt} and Ca are rescaled appropriately with R, our solutions collapse onto a single curve as shown in Figure 4.3.8. The rescaled parameters, denoted with tildes, are

$$\Delta\widetilde{a}_{\text{opt}} \equiv \frac{\Delta a_{\text{opt}}}{R^2} \equiv \frac{2 - a_{\text{opt}}}{R^2}, \tag{4.3.2}$$

$$\widetilde{\text{Ca}} \equiv \frac{\text{Ca}}{R}, \tag{4.3.3}$$

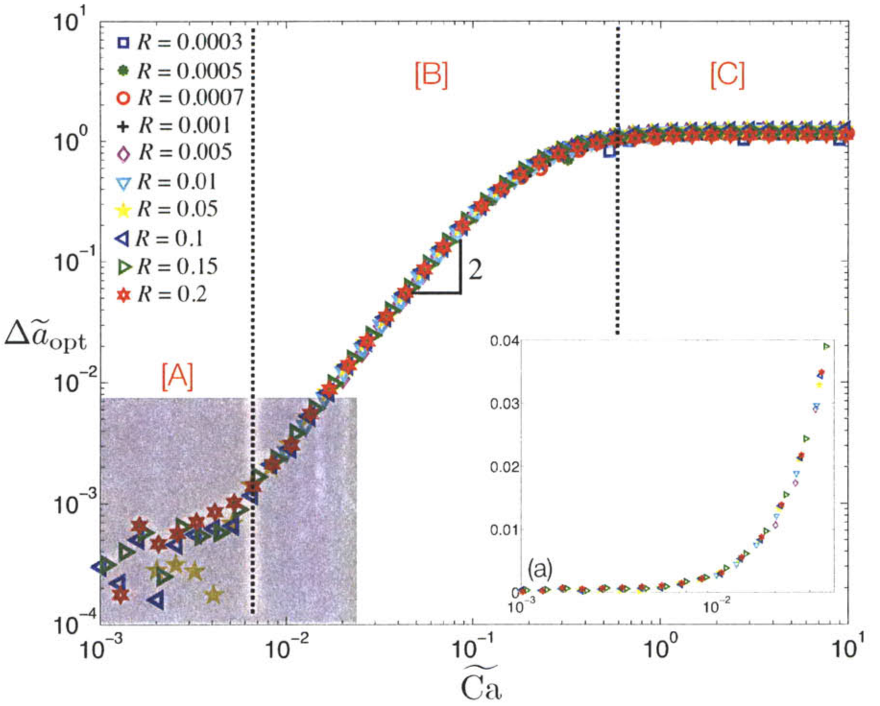

Figure 4.3.7: The deviation from the flat interface, $2 - a_{\text{opt}}$, is denoted as $\Delta\widetilde{a}_{\text{opt}}$ after it has been scaled by R^2. Similarly, $\widetilde{\text{Ca}} \equiv \frac{\text{Ca}}{R}$ is the rescaled capillary number. This particular pair of rescaling results in collapsing Δa_{opt} versus Ca plots into one curve, from which one can extract interesting scaling relations. (The numerical data for small $\widetilde{\text{Ca}}$ is better shown in the inset (a) on a linear vertical scale.) Three distinct regimes emerge from this plot, denoted as [A], [B], and [C]. The regime [A] corresponds to the flat interface as the optimal free surface shape, and [B] shows the optimal deformation growing with surface tension, while the last regime [C] is the optimal deformation saturated at a maximum value.

where $\Delta\widetilde{a}_{\text{opt}}$ is the rescaled deviation from the flat interface. In Figure 4.3.8, $\Delta\widetilde{a}_{\text{opt}}$ is shown to increase as $\widetilde{\text{Ca}}^2$ at moderate values of $\widetilde{\text{Ca}}$ and then reaches a maximum and remain constant for high $\widetilde{\text{Ca}}$. In this limit of $\widetilde{\text{Ca}} \to \infty$, we see that $\Delta\widetilde{a}_{\text{opt}} \sim$ constant, or in dimensional variables:

$$\Delta a_{\text{opt}} \sim \frac{\widehat{R}^2}{\widehat{h}^2}. \tag{4.3.4}$$

Since Δa_{opt} is a measure of free surface deformation (i.e. $\Delta a_{\text{opt}} = 0$ for zero deformation), Eq. (4.3.4) implies that the optimal deformation is only a function of the swimmer's distance from the interface relative to its size only in this limit, and not of the fluid properties. Specifically, the optimal deformation increases when the swimmer is closer to the interface, consistent with Figure 4.3.4.

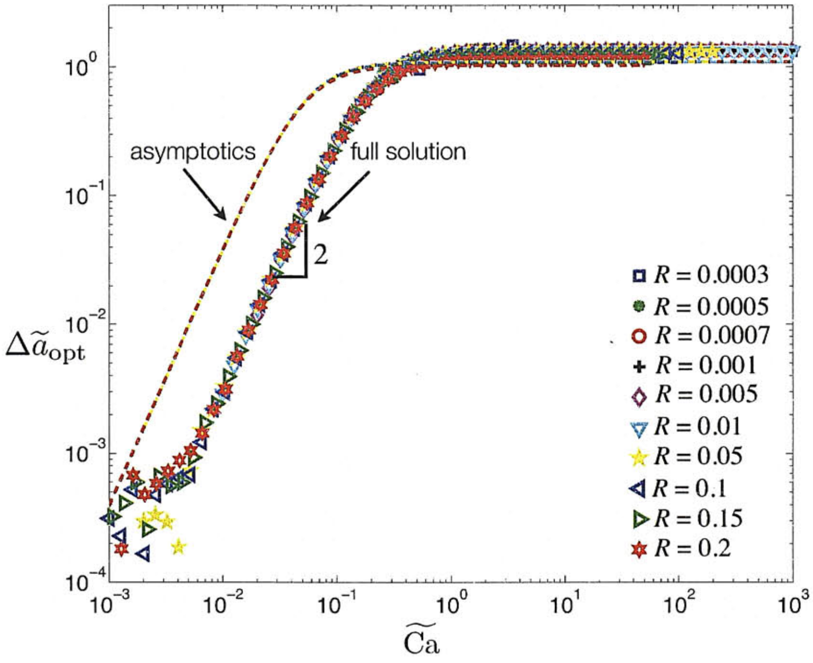

Figure 4.3.8: An approximate expression for $\Delta\widetilde{a}_{\rm opt}$ (plotted as dotted lines) is derived from asymptotic solutions and shows a good overall agreement with the full solutions, despite a clear shift at the transition from flat to deformed interfaces ($\mathrm{Ca}_{\rm crit1}$).

However, this dependency on the relative distance from the interface does not appear at moderate $\widetilde{\rm Ca}$ at which $\Delta\widetilde{a}_{\rm opt} \sim \widetilde{\rm Ca}^2$, or equivalently,

$$\Delta a_{\rm opt} \sim \frac{\mu^2 \widehat{U}^2}{\sigma^2}. \tag{4.3.5}$$

As the optimal free surface shapes transition from flat to deformed, they exhibit a stronger dependence on surface tension, viscosity, and the swimmer speed. These simple scaling relations are useful in providing a rough picture of the underlying physics; however, a more detailed examination of our results can follow by deriving an approximate expression for this function $\Delta\widetilde{a}_{\text{opt}}$ in terms of R and $\widetilde{\text{Ca}}$:

$$\Delta\widetilde{a}_{\text{opt}} = \frac{24R^2 + 52.8}{18R^4 + 103.92R^2 + \frac{0.1352}{\widetilde{\text{Ca}}^2} + 48}. \tag{4.3.6}$$

This optimal deflection (derived from asymptotics) is plotted in Figure 4.3.8 as a set of dotted lines on top of the full solution for comparison. Although it consistently predicts the initial transition point from the flat interface to the deformed (Ca_{crit1}) below the actual value, this approximate solution effectively captures the overall trend of the optimal deformation and also accurately predicts the maximum value of $\Delta\widetilde{a}_{\text{opt}}$.

With the mathematical tools in place, one can delve into the physical implications of the three distinct regimes of the optimal free surface shapes as shown in Figure 4.3.7. The first regime [A] marked by $\widetilde{\text{Ca}} \equiv \frac{\text{Ca}}{R} < 10^{-3}$ corresponds to the optimal free surface being flat, or $\Delta a_{\text{opt}} \longrightarrow 0$. Not surprisingly, the limit of high surface tension (or low Ca) falls in this regime. Furthermore, regardless of Ca, the limit of $R \equiv \frac{\widehat{R}}{h} \longrightarrow 0$ also corresponds to this flat interface case. Since $\widehat{R}$ can be interpreted as the finite size of the swimmer, this result implies that if a swimmer is sufficiently small, or equivalently, sufficiently far from the interface, the undeformed interface results in the most efficient locomotion, regardless of the fluid properties.

The second regime to consider (denoted as [C] in Figure 4.3.7) is $\widetilde{\text{Ca}} \gtrsim 1$ when the deformation reaches its maximum size, and corresponds to low surface tension:

$$\Delta a_{\text{opt}} = \frac{24R^4 + 52.8R}{18R^4 + 103.92R^2 + 48}. \tag{4.3.7}$$

It is important to note that even in the limit of zero surface tension, as long as $R \longrightarrow 0$, the optimal free surface shape remains flat. Finally, the last regime of interest [B] falls between the two said regimes and holds a power law relation of $\Delta a_{\text{opt}} \sim \text{Ca}^2$, as discussed earlier. This power law is valid for the values of $\widetilde{\text{Ca}}$ ranging from 10^{-2} to 10^{-1}, corresponding to moderate values of the capillary number and R.

4.4 Discussion

We have investigated the motion of a low Reynolds swimmer near a free surface thanks to conformal map techniques that yield exact solutions even for large interfacial deformations. With these known solutions, we are able to study the energetic cost of such locomotion and the shapes of the free surface associated with optimal swimming. At mid to high Reynolds numbers, swimming near free surfaces tends to increase drag on the swimmer due to the energy cost associated with generating surface waves. However, for a low Reynolds number swimmer, the presence of the free surface may be beneficial.

Our study quantifies this difference by considering swimmers that *utilize* the free surface to obtain a steady state translation. Within this framework, we find that proximity to the interface increases efficiency. More specifically, the rate of minimum dissipation scales as $\widehat{h}^4$, where $\widehat{h}$ is the swimmer's distance from the interface. This total dissipation does not depend explicitly on surface tension, but instead, is proportional to the square of viscosity μ and the translation speed $\widehat{U}$.

Given that our swimmer's locomotion relies on the presence of the free surface, but not on its deformation, it is an interesting exercise to classify the optimal shapes of the free surface. The optimal free surface shapes, in general, are left-right symmetric and are pulled toward the swimmer. As a function of *increasing* capillary number Ca, the free surface initially stays flat and at some critical Ca, forms a symmetric bump down toward the swimmer. This bump size increases as σ^{-2}, where σ is surface tension, but saturates when Ca reaches its second critical value. In this limit, the optimal deformation size is shown to be inversely proportional to the swimmer's distance from the interface to the second power, $\widehat{h}^2$. We also perform a small perturbation analysis of the full solutions and show that these approximations work remarkably well in this simple limit.

The study of optimal swimming near the air-water interface can be extended in various ways. For instance, one may improve the way we regularize the total dissipation in the fluid by considering the two regimes (near versus far fields) separately and matching them. More importantly, here we have shown only one application of using the exact solutions given by the conformal map. These solutions can be improved by including a finite body of the swimmer. One can also broaden this study by considering different types of surfaces in order to provide a theoretical basis for understanding and controlling low Reynolds number locomotion, in geometries where the swimmer has the ability to modify its environment.

Chapter 5

Conclusion

Our investigation of free surface swimming was first inspired by water snails that exhibit a very peculiar form of locomotion. Separated from the free surface by a thin layer of viscous mucus, these snails use surface tension to drive a flow in their mucus, leading to propulsion. Extending this interplay between the free surface and the swimmer's motion to a general low Reynolds swimmer was motivated by a recent renewal of scientific interest in low Reynolds locomotion, driven by applications in biology and engineering. Although low Reynolds number locomotion is a fairly well studied problem, a mathematical model that includes the free surface has not been offered, apart from the work by Trouilloud *et al.* [71]. While their work focuses specifically on overcoming the Scallop Theorem by deforming the free surface asymmetrically in the limit of asymptotically small perturbations of the interface, we are interested in the steady state motion of a swimmer that breaks symmetry by the presence of the free surface, not necessarily by deformations. Considering the swimmer in this manner allows us to avoid the unsteady nature pertaining to the Scallop Theorem and focus on a general swimmer translating beneath a free surface. Large deformations of the swimmer are captured *exactly* using the conformal mapping techniques.

Following the study of swimming mechanism, the question of optimization arises naturally in investigating locomotion of any biological system. While it is not possible to fully understand the motivation of a given organism in adapting its locomotive strategy, one relevant conjecture is that the swimmer is interested in preserving energy since a biological organism's power generation is constrained physiologically. Based on this idea, we considered how a low Reynolds number swimmer exploits the free surface to propel itself while minimizing the viscous dissipation. The questions we asked range from fundamental — "is the proximity to the interface beneficial for the swimmer?" — to more specific, regarding the optimal shape of the interface. Our results show that the swimmer dissipates less energy by being closer to the free surface. In addition, apart from the cases of extremely high surface tension and the swimmer being far away from the interface (relative to its body size), it is favorable for the swimmer to pull the interface symmetrically toward itself. In a physical context, for most micoorganisms swimming in a mucus-like fluid, the capillary number is sufficiently low (high surface tension) and their body length is sufficiently small that no deformation of the free surface is the most optimal solution for their locomotion. However, one needs to be aware of two important limits in our formulation. First, our model cannot capture accurately the asymptotic limit of the swimmer approaching the free surface, since the singularity description of the swimmer requires that the swimmer be sufficiently far from the interface. More fundamentally, our swimmer is modeled to generate only a completely symmetric "squirming" motion, guaranteeing that its only means to break symmetry comes from its interaction with the free surface. While this is an effective way to isolate the dynamics between the free surface and the swimmer motion, this also biases the presence of the free surface to be energetically favorable for the swimmer. In other words, it may be possible for a general low Reynolds swimmer that is unaware of the usefulness of the free surface to find the presence of the free surface hinders its motion and hence is energetically unfavorable.

We here hope to have painted a comprehensive picture of low Reynolds locomotion near free surfaces, starting with a specific organism and generalizing it to "small" swimmers that rely on a free surface to move, and investigating the role of this environmental factor in locomotive efficiency. In the larger context of low Reynolds number locomotion, we have demonstrated a mathematical framework to model a swimmer in complicated geometries that interact with the swimmer in a nonlinear fashion. For instance, one may analyze the motion of a microorganism near a deformable (elastic) solid boundary as a way to understand how a sperm travels inside the reproductive system. Such modeling approaches, coupled with a scientist's curiosity, can be instrumental in understanding the rich physics still to be uncovered in low Reynolds locomotion.

Appendix A

Details from the point swimmer

A.1 Far field condition

Differentiating the boundary z along the arclength s corresponds to

$$\frac{dz}{ds} = \frac{\mathrm{i}\zeta z_\zeta}{|z_\zeta|}. \tag{A.1.1}$$

In particular, as $\zeta \to -\mathrm{i}$, it can be shown that

$$\frac{dz}{ds} \to -\frac{a}{|a|}. \tag{A.1.2}$$

Then, the stress boundary condition (3.2.8) at infinity becomes

$$f_\infty + \overline{g_\infty} = \frac{\mathrm{i}}{2\mathrm{Ca}} \frac{a}{|a|}. \tag{A.1.3}$$

Since $|\zeta| = 1$, the conjugate of z, $\overline{z(\zeta)}$, is equivalent to $\overline{z}(1/\zeta)$; in the limit of $\zeta \to -\mathrm{i}$, $\overline{z}(1/\zeta)$ reduces to

$$\overline{z} = \overline{z}(\zeta^{-1}) = \frac{\overline{a}\zeta}{1 - \mathrm{i}\zeta} + \overline{a_0} + \frac{\overline{a_1}}{\zeta} = \frac{\overline{a}}{\zeta + \mathrm{i}} + \mathrm{i}\overline{a} + \overline{a_0} + \frac{\overline{a_1}}{\zeta} \to \frac{\overline{a}z}{a} + \ldots. \tag{A.1.4}$$

Recalling the steady state boundary condition

$$\bar{z}f(z) + g(z) = 0, \tag{A.1.5}$$

and the far-field behaviors of $f(z)$ and $g(z)$,

$$f(z) \to f_\infty + \frac{f_\infty^{(1)}}{z} + \dots \qquad \text{and} \qquad g'(z) \to g_\infty + \frac{g_\infty^{(1)}}{z} + \dots, \tag{A.1.6}$$

one can now relate g_∞ to f_∞ as

$$g_\infty = -\frac{f_\infty \bar{a}}{a}. \tag{A.1.7}$$

From the far-field velocity condition (3.4.8), it follows that

$$-f_\infty - \frac{\overline{f_\infty} a}{\bar{a}} = 1. \tag{A.1.8}$$

In order to ensure that this velocity is purely real, a needs to be real as well, leading Eq. (A.1.8) to

$$-f_\infty - \overline{f_\infty} = 1. \tag{A.1.9}$$

Furthermore, combining equations (A.1.3) and (A.1.7) yields

$$f_\infty - \overline{f_\infty} = \frac{\mathrm{i}}{2\mathrm{Ca}}, \tag{A.1.10}$$

which results in (3.4.9), or

$$f_\infty = -\frac{1}{2} + \frac{\mathrm{i}}{4\mathrm{Ca}} \qquad \text{and} \qquad g_\infty = \frac{1}{2} - \frac{\mathrm{i}}{4\mathrm{Ca}}. \tag{A.1.11}$$

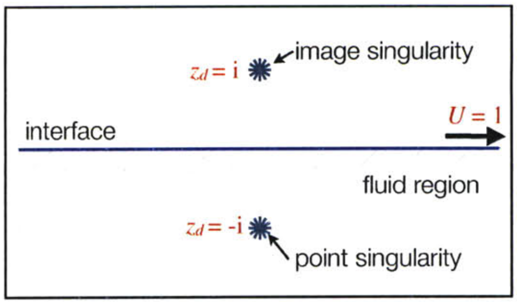

Figure A.2.1: The method of images: to satisfy the boundary condition on the free surface an image singularity must be introduced at the reflection of the point swimmer position.

A.2 Steady swimming beneath a flat interface: method of images

We use the method of images to analyze the motion of a point swimmer translating at $U = -1$ near a flat interface. For convenience, we work in the frame of reference moving with the swimmer, which allows the local velocity at the swimmer's position $z_d = -\mathrm{i}$ to vanish.

The function, $f(z)$, is expected to be in the following form

$$f(z) = \frac{s^*}{z+\mathrm{i}} + \frac{\hat{s^*}}{z-\mathrm{i}} + f_0 \tag{A.2.1}$$

which consists of an image stresslet at $z = \mathrm{i}$, in addition to the stresslet at $z = -\mathrm{i}$ (see Figure A.2.1). These singularities, as well as the constant f_0, need to be calculated. By the stress boundary condition (3.2.8) on $\overline{z} = z$, $g'(z)$ is related to $f(z)$ by

$$\overline{g}'(z) = -f(z) - z\overline{f}'(z) + \frac{\mathrm{i}}{2\mathrm{Ca}}, \tag{A.2.2}$$

which, when combined with Eq. (A.2.1), becomes

$$g'(z) = -\frac{\mathrm{i}s^*}{(z+\mathrm{i})^2} + \frac{\mathrm{i}\overline{s^*}}{(z-\mathrm{i})^2} + g_0, \tag{A.2.3}$$

or

$$g'(z) = \left[\frac{\mathrm{i}s^*}{(z+\mathrm{i})^2} - \frac{\mathrm{i}\overline{s^*}}{(z-\mathrm{i})^2} \right] - \frac{2\mathrm{i}s^*}{(z+\mathrm{i})^2} + \frac{2\mathrm{i}\overline{s^*}}{(z-\mathrm{i})^2} + g_0. \tag{A.2.4}$$

The velocity in the far-field must be 1 in the co-moving frame of reference. Substituting equations (A.2.1) and (A.2.2) in the expression for the velocity (3.2.3) at infinity produces the following condition:

$$-f_0 + \overline{g_0} = 1. \tag{A.2.5}$$

Then, one can collect the constant terms in the stress condition (A.2.2) to find

$$f_0 = -\frac{1}{2} + \frac{\mathrm{i}}{4\mathrm{Ca}}, \quad g_0 = \frac{1}{2} - \frac{\mathrm{i}}{4\mathrm{Ca}}. \tag{A.2.6}$$

Going back to the swimmer, the finite part of the swimmer velocity must be zero, meaning

$$0 = -\frac{\overline{s^*}}{(-2\mathrm{i})} - f_0 + \frac{\mathrm{i}s^*}{(-4)} - \frac{\mathrm{i}s^*}{(-4)} + \overline{g_0} \tag{A.2.7}$$

so that

$$s^* = 2\mathrm{i}. \tag{A.2.8}$$

With the functions $f(z)$ and $g'(z)$ known, everything about the flow is also known. Furthermore, the condition that the free surface is a streamline can be verified by using Eqs. (A.2.1) and (A.2.2):

$$\begin{aligned} g(z) + zf(z) &= \frac{is^*}{(z+\mathrm{i})} - \frac{\mathrm{i}\overline{s^*}}{(z-\mathrm{i})} + zg_0 + \frac{zs^*}{(z+\mathrm{i})} + \frac{z\overline{s^*}}{(z-\mathrm{i})} + zf_0 && \text{(A.2.9)} \\ &= 2\mathrm{Re}[s^*] = 0. && \text{(A.2.10)} \end{aligned}$$

In summary, we have shown that a point singularity can translate steadily with a unit horizontal speed underneath a flat free surface (at any capillary number) if it is a point stresslet of strength 2i with a superposed potential dipole of strength $2\mathrm{i}s^* = -4$. It is noteworthy that this solution is not limited to the case of $\mathrm{Ca} \ll 1$ in which one would expect interfaces to remain flat. Instead, we solve for singularities (i.e., stresslet and potential dipole) that would yield a steady motion while keeping the free surface flat, regardless of how deformable the surface is. Not surprisingly, the result is shown to be independent of the capillary number because the curvature of the flat interface is everywhere zero. For a deformed interface, however, the capillary number plays a crucial role.

Appendix B

Calculating the rate of viscous dissipation

Taking the scalar product of the well-known Stokes questions,

$$\nabla \widehat{p} = \mu \nabla^2 \mathbf{u}, \tag{B.0.1}$$

with the fluid velocity $\mathbf{u}$ and integrating over the entire domain D produces the following expression for the rate of work:

$$0 = \iint\limits_{D} \left[-\mathbf{u} \cdot \nabla \widehat{p} + \mu \mathbf{u} \cdot \nabla^2 \mathbf{u} \right] \, d\widehat{V}. \tag{B.0.2}$$

After some manipulation, this can be rewritten in the index notation as

$$0 = \oint\limits_{\partial D} \widehat{u}_j \left(-\widehat{p} n_j + 2\mu \widehat{e}_{ij} n_j \right) \, d\widehat{s} - 2\mu \iint\limits_{D} \widehat{e}_{ij}^2 \, d\widehat{V}, \tag{B.0.3}$$

where ∂D corresponds to the surface of the fluid domain and $\widehat{e}_{ij} \equiv \frac{1}{2}(\frac{\partial \widehat{u}_i}{\partial \widehat{x}_j} + \frac{\partial \widehat{u}_j}{\partial \widehat{x}_i})$ is the strain rate tensor. Keep in mind that the Gauss' theorem allows the first integral in Eq. (B.0.3) to become a surface integral. Non-dimensionalizing the equations and recognizing that the ∂D consists of both the free surface and the "hole" of radius R

around the swimmer, Eq. (B.0.3)s reduces to

$$0 = \sigma\widehat{U} \oint\limits_{\partial D_{\text{int}}} \kappa\mathbf{u}\cdot\mathbf{n}\; ds - \mu\widehat{U}^2 \oint\limits_{\partial D_{\text{swim}}} u_j\left(-pn_j + 2e_{ij}n_j\right)\; ds - 2\mu\widehat{U}^2 \iint\limits_{D} e_{ij}^2\; dV, \tag{B.0.4}$$

where $\partial D \equiv \partial D_{\text{int}} - \partial D_{\text{swim}}$. Note that the first integrand has been replaced by the equivalent expression for the curvature on the free surface, while a minus sign in front of the swimmer surface integral is necessary in order to keep the positive orientation. In the physical context, this particular surface integral can be considered the amount of work generated by the swimmer, or $\widehat{\phi}$ in the dimensional form:

$$\widehat{\phi} \equiv \left|\mu\widehat{U}^2 \oint\limits_{\partial D_{\text{swim}}} u_j\left(-pn_j + 2e_{ij}n_j\right)\; ds\right| = \left|\sigma\widehat{U} \oint\limits_{\partial D_{\text{int}}} \kappa\mathbf{u}\cdot\mathbf{n}\; ds - 2\mu\widehat{U}^2 \iint\limits_{D} e_{ij}^2\; dV\right|. \tag{B.0.5}$$

After $\widehat{\phi}$ is scaled by $\mu\widehat{U}^2$, the typical expression for the swimmer power in an unbounded Stokes flow, one obtains

$$\phi = \left|\frac{1}{\text{Ca}} \oint\limits_{\partial D_{\text{int}}} \kappa\mathbf{u}\cdot\mathbf{n}\; ds - 2\iint\limits_{D} e_{ij}^2\; dV\right|. \tag{B.0.6}$$

Now the first integral in Eq. (B.0.6) is shown to vanish, indicating that there is no time rate of change in work the swimmer generates to deform the free surface. This bodes well with our steady state description of the problem in which the free surface shape does not evolve in time. The second integrand can be expressed in terms of our known solutions, $f(z)$ and $g(z)$:

$$e_{ij}^2 = \frac{\partial}{\partial\overline{z}}\left[zf''(\overline{z}\,\overline{f}' - \overline{f}) + zg''\overline{f}' + g''\overline{g}'\right] + \frac{\partial}{\partial z}\left[\overline{z}\,\overline{g}''f'\right], \tag{B.0.7}$$

based on $e_{11} + \mathrm{i}e_{12} = \overline{g''(z)} + z\overline{f''(z)}$.

Recalling the complex form of the divergence theorem, one can turn Eq. (B.0.7) into two separate surface integrals,

$$\iint\limits_{D} e_{ij}^2 \, dV = \frac{1}{2i} \oint\limits_{\partial D} \left[z\overline{z} f'' \overline{f'} - z f'' \overline{f} + z g'' \overline{f'} + g'' \overline{g'} \right] dz - \frac{1}{2i} \oint\limits_{\partial D} \overline{z g''} f' d\overline{z}. \tag{B.0.8}$$

This above expression corresponds to the rate of work generated by the swimmer, ϕ, or equivalently, the rate of total dissipation, E, in the fluid domain. We then solve for the free surface shapes that minimize this quantity (or yield E_{min}) in Chapter 4.

Appendix C

Details from the optimization

C.1 Full equations

The complex functions F and G that describe the physical system exactly are determined by a pair of complex constants, $C = C_x + \mathrm{i}C_y$ and $D = D_x + \mathrm{i}D_y$, as shown below:

$$D_x = \frac{1}{m_0}\left[m_1\left(\frac{1}{a} + \frac{1}{\mathrm{Ca}}\mathrm{Re}(\mathrm{i}I_{\zeta\zeta}(-\mathrm{i}))\right) + \frac{m_2}{\mathrm{Ca}}\mathrm{i}I_{\zeta}(-\mathrm{i}) + \frac{m_3}{\mathrm{Ca}}\right], \tag{C.1.1}$$

$$D_y = \frac{1}{m_0}\left[m_4\left(\frac{1}{a} + \frac{1}{\mathrm{Ca}}\mathrm{Re}(\mathrm{i}I_{\zeta\zeta}(-\mathrm{i}))\right) + \frac{m_5}{\mathrm{Ca}}\mathrm{i}I_{\zeta}(-\mathrm{i}) + \frac{m_6}{\mathrm{Ca}}\right], \tag{C.1.2}$$

$$C_x = 4D_y - \frac{1}{2\mathrm{Ca}}\mathrm{Re}(\mathrm{i}I_{\zeta\zeta}(-\mathrm{i})) - \frac{1}{2a}, \tag{C.1.3}$$

$$C_y = -2D_x + \frac{\mathrm{i}}{2\mathrm{Ca}}I_{\zeta}(-\mathrm{i}), \tag{C.1.4}$$

$$m_o = \mathrm{Im}\left[4a^2\mathrm{i}\left(1 - \frac{\overline{a_1}}{a_1} - \frac{aa_3}{a_1^2}\right)\left(1 - \frac{a_1}{\overline{a_1}} + \frac{a^2}{2\overline{a_1}^2}\right)\right], \tag{C.1.5}$$

$$m_1 = \mathrm{Im}\left[-\frac{2a^3}{\overline{a_1}}\left(1 + \frac{\frac{5a}{2} + 1 - \mathrm{i}c}{a_1} + \frac{a(\mathrm{i}c - 1)}{a_1^2}\right)\left(1 + \frac{\overline{a_2}}{2\overline{a_1}}\right)\right], \tag{C.1.6}$$

$$m_2 = \mathrm{Im}\left[\frac{4a^2\mathrm{i}}{\overline{a_1}}\left(1 + \mathrm{i}c + \frac{a\overline{a_2}}{4\overline{a_1}}\right)\left(1 - \frac{aa_3}{a_1^2} - \frac{\overline{a_1}}{a_1}\right)\right], \tag{C.1.7}$$

$$m_3 = \mathrm{Im}\left[2a\overline{a_2}I_\zeta(0)\left(1 - \mathrm{i}a\left(\frac{1}{\overline{a_2}} - \frac{2}{\overline{a_1}}\right)\frac{I(0) - I(-\mathrm{i})}{I_\zeta(0)}\right)\left(1 - \frac{aa_3}{a_1^2} - \frac{\overline{a_1}}{a_1}\right)\right], \tag{C.1.8}$$

$$m_4 = \mathrm{Im}\left[-\frac{2a^3\mathrm{i}}{a_1}\left(1 + \frac{a_2}{2a_1}\right)\left(1 - \frac{a_1}{\overline{a_1}} + \frac{a^2}{2\overline{a_1}^2}\right)\right], \tag{C.1.9}$$

$$m_5 = \mathrm{Im}\left[\frac{4a^2\mathrm{i}}{a_1}\left(1 - \mathrm{i}c + \frac{aa_2}{4a_1}\right)\left(1 - \frac{3(\frac{a}{2} + 1 + \mathrm{i}c)}{\overline{a_1}} + \frac{a(\mathrm{i}c + 1)}{\overline{a_1}^2}\right)\right], \tag{C.1.10}$$

$$m_6 = \mathrm{Im}\left[2aa_2\overline{I_\zeta(0)}\mathrm{i}\left(1 + \mathrm{i}a\left(\frac{1}{a_2} - \frac{2}{a_1}\right)\frac{\overline{(I(0) - I(-\mathrm{i}))}}{\overline{I_\zeta(0)}}\right)\left(1 - \frac{a_1}{\overline{a_1}} + \frac{a^2}{2\overline{a_1}^2}\right)\right], \tag{C.1.11}$$

where

$$a_1 = \frac{3a}{2} - 1 - \mathrm{i}c, \tag{C.1.12}$$

$$a_2 = \frac{a}{2} - 1 + \mathrm{i}c, \tag{C.1.13}$$

$$a_3 = a - 1 + \mathrm{i}c. \tag{C.1.14}$$

Since they are often very long and complicated functions of the conformal map, or the shape parameters, a and c, obtaining physically relevant information from C and D often proves to be a fruitless task. However, in the case of symmetric deformations

$(c \equiv 0)$, C and D reduce to

$$C_x = \frac{6a-5}{2a(a-1)}, \tag{C.1.15}$$

$$C_y = \frac{1}{\mathrm{Ca}}\left[\left(-2b_1 + \frac{1}{2}\right)\mathrm{i}I_\zeta(-\mathrm{i}) - 2b_2\right], \tag{C.1.16}$$

$$D_x = \frac{1}{\mathrm{Ca}}\left[b_1 \mathrm{i} I_\zeta(-\mathrm{i}) + b_2\right], \tag{C.1.17}$$

$$D_y = \frac{7a-6}{8a(a-1)}, \tag{C.1.18}$$

where

$$I(\zeta) = \frac{1}{8\pi}\oint_{|\zeta'|=1} \frac{d\zeta'}{\zeta'}\frac{\zeta'+\zeta}{\zeta'-\zeta}\frac{1}{|z_\zeta(\zeta')|}, \tag{C.1.19}$$

$$b_1 = \frac{a}{4(a-1)} + \frac{(3a-2)(3a-4)}{4a^2(a-1)}, \tag{C.1.20}$$

$$b_2 = \mathrm{Im}(I_\zeta(0))\frac{(3a-2)^2(a-2)}{8a^3} - (I(0) - I(-\mathrm{i}))\frac{(3a-2)(a+2)}{4a^2}. \tag{C.1.21}$$

Apart from the integral $I(\zeta)$ that needs to be solved numerically, C and D are now relatively simple functions of a. Since the optimal free surface shapes are found to be approximately symmetric $(c \approx 0)$, these equations can be studied more closely to help understand results found in Chapter 4.

C.1.1 Asymptotics

Keeping $c \equiv 0$, we now consider asymptotically small symmetric deformations. By setting $a = 2 + \varepsilon + O(\varepsilon^2)$, we obtain

$$C_x = \frac{7}{4} + \varepsilon C_x^{(1)} + O(\varepsilon^2), \tag{C.1.22}$$

$$C_y = \frac{1}{8\mathrm{Ca}} + \varepsilon C_y^{(1)} + O(\varepsilon^2), \tag{C.1.23}$$

$$D_x = \varepsilon D_x^{(1)} + O(\varepsilon^2), \tag{C.1.24}$$

$$D_y = \frac{1}{2} + \varepsilon D_y^{(1)} + O(\varepsilon^2). \tag{C.1.25}$$

Furthermore, a simplified expression for the rate of dissipation is obtained by considering the singularities that satisfy our optimal solutions in an *unbounded* fluid domain.

$$E = \frac{12|q^*|^2}{R^6} + \frac{2|d|^2}{R^4} + |s^*|^2\left(\frac{2}{R^4} + \frac{4}{R^2}\right) + \frac{1}{R^4}\left(12\mathrm{Re}(\overline{s^*}q^*) + 4\mathrm{Im}(\overline{s^*}d)\right), \qquad \text{(C.1.26)}$$

and

$$s^* = \frac{(3a-2)^2}{4}D, \qquad \text{(C.1.27)}$$
$$d = -\frac{3a-2}{8}\left[2\mathrm{i}D(a^2-3a-2) + C(3a^2-8a+4)\right], \qquad \text{(C.1.28)}$$
$$q^* = -\frac{(a-2)(3a-2)^3}{16}D, \qquad \text{(C.1.29)}$$

where s^*, d, and q^* are stresslet, dipole, and quadrupole singularities, respectively. Although this simplified expression for the viscous dissipation rate, E, does not fully capture the effect of the free surface, the resulting trends are shown to correspond remarkably well to the full expression. Now E is perturbed in the limit of small surface deformations to yield:

$$E^{(0)} = 8\left(\frac{4}{R^4} + \frac{2}{R^2}\right). \qquad \text{(C.1.30)}$$
$$E^{(1)} = (D_y^{(0)})^2\left(\frac{64}{R^4} + \frac{192}{R^2}\right) + D_y^{(0)}D_y^{(1)}\left(\frac{208}{R^4} + \frac{2}{R^2}\right) + D_y^{(0)}C_x^{(0)}\frac{64}{R^4}, \qquad \text{(C.1.31)}$$
$$\begin{aligned} E^{(2)} = {} & (D_y^{(0)})^2\left(\frac{192}{R^6} - \frac{512}{R^4} + \frac{408}{R^2}\right) + |C^{(0)}|^2\frac{8}{R^4} + |D^{(1)}|^2\left(\frac{128}{R^4} + \frac{64}{R^2}\right) \\ & + D_y^{(0)}D_y^{(1)}\left(\frac{128}{R^4} + \frac{384}{R^2}\right) + D_y^{(0)}D_y^{(2)}\left(\frac{256}{R^4} + \frac{128}{R^2}\right) + D_y^{(0)}C_x^{(0)}\frac{224}{R^4} \\ & + (D_y^{(0)}C_x^{(1)} - D_y^{(1)}C_y^{(0)} + D_y^{(1)}C_x^{(0)})\frac{64}{R^4}, \end{aligned} \qquad \text{(C.1.32)}$$

where $E \equiv E^{(0)} + \varepsilon E^{(1)} + \varepsilon^2 E^{(2)} + O(\varepsilon^3)$, with $E^{(0)}$ corresponding to the rate of the viscous dissipation in the limit of a flat interface. Note that the dependence on Ca comes in through $D_x^{(1)}$ and $C_y^{(0)}$, both of which appear only at $O(\varepsilon^2)$.

Critical capillary numbers

One needs to consider the asymptotic solution at $O(\varepsilon^2)$ to explore the dependence on Ca. As shown in Figure 4.3.3, $\mathrm{Ca}_{\mathrm{crit1}}$ is the transition point from the flat state to the deformed state, while $\mathrm{Ca}_{\mathrm{crit2}}$ corresponds to the capillary number at which the maximum optimal deformation is reached. In particular, the initial transition ($\mathrm{Ca}_{\mathrm{crit1}}$) can be fairly well predicted by considering the asymptotic solution to $O(\varepsilon^2)$ as a function of varying R. In Figure C.1.1, $\mathrm{Ca}_{\mathrm{crit1}}$ for both the full solution and asymptotics is shown to increase linearly with R, while the asymptotic solution consistently yields lower values of $\mathrm{Ca}_{\mathrm{crit1}}$. Such discrepancy is to be expected not only due to the nature of asymptotic analysis but also due to the imprecise way we extract the critical capillary numbers from the full solution. The critical capillary numbers are obtained by fitting linear functions to three distinct regions of a_{opt} (see the inset of Figure 4.3.3) and calculating where they intercept. Despite that, the close correspondence especially in the general trend between the full and the analytic solutions demonstrates the usefulness of investigating the small perturbation limits.

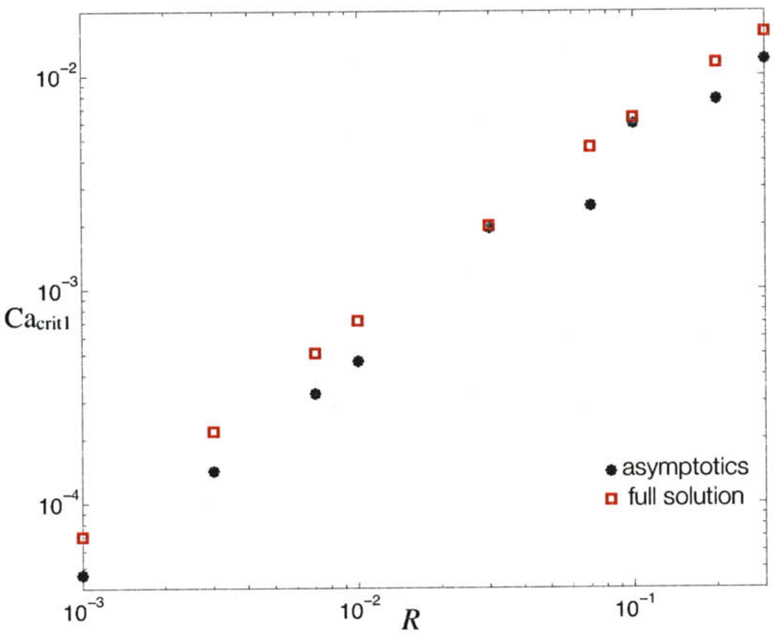

Figure C.1.1: Considering the asymptotic solutions to $O(\varepsilon^2)$ allows one to predict the values of $\mathrm{Ca}_{\mathrm{crit}1}$ for varying R, as plotted here. (The solid dots correspond to the asymptotic equations, while the empty squares are the full results.) The asymptotic solutions are in a good agreement with the exact equations, but they tend to be consistently lower.

Bibliography

[1] R. Altendorfer, N. Moore, H. Komsuoglu, M. Buehler, H. B. Brown, D. McMordie, U. Saranli, R. Full, and D. E. Koditschek. Rhex: A biologically inspired hexapod runner. *Auton. Robot.*, 11:207–213, 2001.

[2] W. P. Aspey and J. E. Blankenship. Aplysia behavioral biology: I. A multivariate analysis of burrowing in *A. Brasiliana. Behav. Biol.*, 17:279–299, 1976.

[3] W. P. Aspey and J. E. Blankenship. Aplysia behavioral biology: II. induced burrowing in swimming *A. Brasiliana* by burrowed conspecifics. *Behav. Biol.*, 19:301–312, 1976.

[4] T. Audesirk and G. Audesirk. *"Behavior of Gastropod Molluscs" in The Mollusca*, volume 8, chapter 1, pages 59–64. Academic Press, inc., 1985.

[5] J. E. Avron, O. Gat, and O. Kenneth. Optimal swimming at low reynolds numbers. *Phys. Rev. Lett.*, 93:186001, 2004.

[6] M. Z. Bazant and D. G. Crowdy. *Handbook of Materials Modelling, Vol I, 4.10,* chapter Conformal mapping methods for interfacial dynamics. Springer, 2005.

[7] L. E. Becker, S. A. Koehler, and H. A. Stone. On self-propulsion of micro-machines at low reynolds number: Purcell's three-link swimmer. *J. Fluid Mech.*, 490:15–45, 2003.

[8] N. Benjanuvatra, G. Dawson, B. A. Blanksby, and B. C. Elliott. Comparison of buoyancy, passive and net active drag forces between fastskin and standard swimsuits. *J. Sci. Med. Sport.*, 5:115–123, 2002.

[9] C. Berdan and L. G. Leal. Motion of a sphere in the presence of a deformable interface. Part I. Perturbation of the interface from flat: the effects of drag and torque. *J. Colloid Interface Sci.*, 87:62, 1982.

[10] H.C. Berg. Dynamic properties of bacterial flagellarl motors. *Nature*, 249:77–79, 1974.

[11] J. M. Birch and M. H. Dickinson. Spanwise flow and the attachment of the leading-edge vortex on insect wings. *Nature*, 412:729–733, 2001.

[12] J. R. Blake. A spherical evelope approach to ciliary propulsion. *J. Fluid Mech.*, 46:199–208, 1971.

[13] C. Brennen and H. Winet. Fluid mechanics of propulsion by cilia and flagella. *Annu. Rev. Fluid Mech.*, 9:339, 1977.

[14] F. Brocher. Les phénomènes capillaires, leur importance dans la biologie aquatique. *Ann. Biol. Lacustre*, IV:89–139, 1910.

[15] G. F. Carrier, M. Krook, and C. E. Pearson. *Functions of a complex variable.* Hod Books, 1983.

[16] B. Chan, N. J. Balmforth, and A. E. Hosoi. Building a better snail: Lubrication and adhesive locomotion. *Phys. Fluids*, 17:113101, 2005.

[17] J. C. Chatard and B. Wilson. Effect of fastskin suits on performance, drag, and energy cost of swimming. *Med. Sci. Sports Exerc*, 40:1149–1154, 2008.

[18] S. Childress. *Mechanics of Swimming and Flying.* Cambridge University Press, 1981.

[19] M. Copeland. Locomotion in two species of the gastropod genus alectrion with observations on the behavior of pedal cilia. *Biol. Bull.*, 37:126–138, 1919.

[20] M. Copeland. Ciliary and muscular locomotion in the gastropod genus polinices. *Biol. Bull.*, 42:132–142, 1922.

[21] A. Delextrat, T. Bernard, C. Hausswirth, F. Bercruyssen, and J. Brisswalter. Effect of swimming with a wet suit on energy expenditure during subsequent cycling. *J. Appl. Physiol.*, 28:356–369, 2003.

[22] T. G. Deliagina and G. N. Orlovsky. Control of locomotion in the freshwater snail planorbis corneus. I. Locomotory repertoire of the snail. *J. Exp. Biol.*, 152:389–404, 1990.

[23] M. Denny. The role of gastropod pedal mucus in locomotion. *Nature*, 285:160–161, 1980.

[24] M. W. Denny. A quantitative model for the adhesive locomotion of the terrestrial slug, ariolimax columbianus. *J. Exp. Biol.*, 91:195–217, 1981.

[25] R. Dreyfus, J. Baudry, M. L. Roper, M. Fermigier, H. A. Stone, and J. Bibette. Microscopic artificial swimmers. *Nature*, 437:862–865, 2005.

[26] R. H. Ewoldt, C. Clasen, A. E. Hosoi, and G. H. McKinley. Rheological fingerprinting of gastropod pedal mucus and synthetic complex fluids for biomimicking adhesive locomotion. *Soft Matter*, 3:634–643, 2007.

[27] W. M. Farmer. Swimming gastropods (opisthrobranchia and prosobranchia). *Veliger*, 13:73–89, 1970.

[28] P. H. Gaskell, P. K. Jimack, M. Sellier, and H. M. Thompson. Flow of evaporating, gravity-driven thin liquid films over topography. *Phys. Fluids*, 18:013601, 2006.

[29] R. J. Goldacre. Surface films on natural bodies of water. *J. Anim. Ecol.*, 18:36–39, 1949.

[30] R. Goodwin and G. M. Homsy. Viscous flow down a slope in the vicinity of a contact line. *Phys. Fluids A-Fluid*, 3:515–528, 1991.

[31] J. P. Hernandez-Ortiz, C. G. Stoltz, and M. D. Graham. Transport and collective dynamics in suspensions of confined swimming particles. *Phys. Rev. Lett.*, 95:204501, 2005.

[32] H. Hertel. *Structure, form, movement.* New York, Reinhold, 1966.

[33] J. Jeong and H. K. Moffatt. Free-surface cusps associated with flow at low reynolds number. *J. Fluid Mech.*, 241:1–22, 1992.

[34] H. D. Jones and E. R. Trueman. Locomotion of the limpet, *Patella Vulgata L.* *J. Exp. Biol.*, 52:201–216, 1970.

[35] S. Kalliadasis, C. Bielarz, and G. M. Homsy. Steady free-surface thin film flows over topography. *Phys. Fluids*, 12:3305–3305, 2000.

[36] W. E. Langlois. *Slow viscous flow.* Macmillan, 1964.

[37] E. Lauga and A. E. Hosoi. Tuning gastropod locomotion: Modeling the influence of mucus rheology on the cost of crawling. *Phys. Fluids*, 18:113102, 2006.

[38] L. Gary Leal. *Advanced Transport Phenomena: Fluid mechanics and convective trasport processes.* Cambridge University Press, Cambridge, UK, 2007.

[39] S. Lee, J. W. M. Bush, A. E. Hosoi, and Lauga E. Crawling beneath the free surface: Water snail locomotion. *Phys. Fluids*, 20:082106, 2008.

[40] S. H. Lee, R. S. Chadwick, and L. G. Leal. Motion of a sphere in the presence of a plane interface. Part 1. An approximate solution by generalization of the method of lorentz. *J. Fluid Mech.*, 93:705–726, 1979.

[41] S. H. Lee and L. G. Leal. Motion of a sphere in the presence of a plane interface. Part 2. An exact solution in bipolar co-ordinates. *J. Fluid Mech.*, 98:193–224, 1980.

[42] J. Lighthill. Flagellar hydrodynamics. *SIAM Rev.*, 18:161–230, 1976.

[43] M. J. Lighthill. On the squirming motion of nearly spherical deformable bodies through liquids at very small reynolds numbers. *Commun. Pur. Appl. Math.*, 5:109–118, 1952.

[44] H. W. Lissman. The mechanism of locomotion in gastropod molluscs: I. Kinematics. *J. Exp. Biol.*, 21:58–69, 1945.

[45] H. W. Lissman. The mechanism of locomotion in gastropod molluscs: II. Kinetics. *J. Exp. Biol.*, 22:37–50, 1945.

[46] A. Mazouchi and G. M. Homsy. Free surface stokes flow over topography. *Phys. Fluids*, 13:2751–2761, 2001.

[47] L. J. Milne and M. J. Milne. The life of the water film. *The Scientific Monthly*, 66:113–121, 1948.

[48] T. G. Myers. Thin films with high surface tension. *SIAM Rev.*, 40:441–462, 1998.

[49] A. Oron, S. H. Davis, and S. G. Bankoff. Long-scale evolution of thin liquid films. *Rev. Mod. Phys.*, 69:931–980, 1997.

[50] G. H. Parker. The mechanism of locomotion in gastropods. *J. Morphol.*, 22:155, 1911.

[51] T. J. Pedley and J. O. Kessler. Hydrodynamic phenomena in suspensions of swimming microorganisms. *Annu. Rev. Fluid Mech.*, 24:313–358, 1992.

[52] L. M. Peurrung and D. B. Graves. Spin coating over topography. *IEEE T. Semiconductor M.*, 6:72–76, 1993.

[53] R. Playter, M. Buehler, and M. Raibert. BigDog. In *Unmanned Systems Technology VIII. Edited by Gerhart, Grant R.; Shoemaker, Charles M.; Gage, Douglas W.. Proceedings of the SPIE, Volume 6230, pp. 62302O (2006).*, volume 6230 of *Presented at the Society of Photo-Optical Instrumentation Engineers (SPIE) Conference*, 2006.

[54] C. Pozrikidis and S. T. Thoroddsen. The deformation of a liquid-film flowing down an inclined plane wall over a small particle arrested on the wall. *Phys. Fluids*, 3:2546–2558, 1991.

[55] W. G. Pritchard, L. R. Scott, and S. J. Tavener. Numerical and asymptotic methods for certain viscous free-surface flows. *Philos. T. Roy. Soc. A*, 340:1–45, 1992.

[56] E. M. Purcell. Life at low reynolds numbers. *Am. J. Phys.*, 45:3–11, 1977.

[57] O. Reynolds. On the theory of lubrication and its application to Mr. Beauchamp Tower's experiments, including an experimental determination of the viscosity of olive oil. *Philos. T. Roy. Soc.*, 177:157–234, 1886.

[58] R. V. Roy, A. J. Roberts, and M. E. Simpson. A lubrication model of coating flows over a curved substrate in space. *J. Fluid Mech.*, 454:235–261, 2002.

[59] D. Saintillan and M. J. Shelley. Instabilities, pattern formation, and mixing in active suspensions. *Phys. Fluids*, 20, 2008.

[60] L. W. Schwartz and D. E. Weidner. Modeling of coating flows on curved surfaces. *J. Eng. Math.*, 29:91–103, 1995.

[61] A. Shapere and F. Wilczek. Self-propulsion at low reynolds number. *Phys. Rev. Lett.*, 58:2051–2054, 1987.

[62] R. A. Simha and S. Ramaswamy. Hydrodynamic fluctuations and instabilities in ordered suspensions of self-propelled particles. *Phys. Rev. Lett.*, 89, 2002.

[63] H. Simroth. Die bewegung unserer landschnecken, hauptsächlich erörtert an der solhe des,. *Limax. Z. Wiss. Zool*, 22:284, 1879.

[64] R. D. Starling, D. L. Costill, T. A. Trappe, A. C. Jozsi, S. W. Trappe, and B. H. Goodpaster. Effect of swimming suit design on the energy demands of swimming. *Med. Sci. Sports Exerc*, 27:1086–1089, 1995.

[65] L. E. Stillwagon and R. G. Larson. Fundamentals of topographic substrate leveling. *J. Appl. Phys.*, 63:5251–5258, 1988.

[66] L. E. Stillwagon and R. G. Larson. Leveling of thin-films over uneven substrates during spin coating. *Phys. Fluids A-Fluid*, 2:1937–1944, 1990.

[67] D. Tam and A. E. Hosoi. Optimal stroke patterns for purcell's three-link swimmer. *Phys. Rev. Lett.*, 98, 2007.

[68] G. I. Taylor. Analysis of the swimming of microscopic organisms. *R. Soc. London, Ser. A*, 209:447, 1951.

[69] H. M. Toussaint, L. Bruinink, R. Coster, M. De Looze, B. Van Rossem, R. Van Veenen, and G. De Groot. Effect of a triathlon wet suit on drag during swimming. *Med. Sci. Sports Exerc.*, 21:325–328, 1989.

[70] H. M. Toussaint, M. Truijens, M. J. Elzinga, A. van de Ven, H. de Best, B. Snabel, and G. De Groot. Effect of a fast-skin 'body' suit on drag during front crawl swimming. *Sports Biomech.*, 1:1–10, 2002.

[71] R. Trouilloud, T. S. Yu, A. E. Hosoi, and E. Lauga. Soft swimming: Exploiting deformable interfaces for low reynolds number locomotion. *Phys. Rev. Lett.*, 101:048102, 2008.

[72] F. Vlès. Sur les ondes pédiuses des mollosques reptateurs. *Acad. Sci., Paris, C. R.*, 145:276, 1907.